From explosive vent opening to effusive outpouring: mineral constraints on magma dynamics and timescales at Paricutin monogenetic volcano

Patricia Larrea[1,2*], Helena Albert[3,4], Teresa Ubide[5], Fidel Costa[4], Vanessa Colás[6], Elisabeth Widom[2], Claus Siebe[7]

[1]Department of Geology and Andean Geothermal Center of Excellence (CEGA), Facultad de Ciencias Físicas y Matemáticas, Universidad de Chile, Plaza Ercilla 803, Santiago, Chile

[2]Department of Geology & Environmental Earth Science, Miami University, Oxford, OH, USA

[3]Department of Mineralogy, Petrology and Applied Geology, University of Barcelona, Barcelona, Spain

[4]Earth Observatory of Singapore, Nanyang Technological University, Singapore

[5]School of Earth and Environmental Sciences, The University of Queensland, Brisbane, Australia

[6]Dpto. Procesos Litosféricos, Instituto de Geología, Universidad Nacional Autónoma de México, Mexico City, Mexico

[7]Dpto. de Vulcanología, Instituto de Geofísica, Universidad Nacional Autónoma de México, Mexico City, Mexico

*corresponding author:

Tel: +56 965579141

E-mail: plarrea@ing.uchile.cl

ABSTRACT

Paricutin volcano is the youngest monogenetic cone from the Michoacán-Guanajuato volcanic field (Mexico), with an excellent historical eruption record from February 1943 to March 1952. The magma emitted during the nine years of activity was compositionally zoned from basaltic andesite to andesite. This eruption has been considered a classic example of magma differentiation controlled by crustal assimilation combined with fractional crystallization. However, a recent geochemical study of the eruption products points to mantle source heterogeneity and fractional crystallization as the key processes involved in the compositional variability of the magmas. Here we present a detailed petrological characterization of the minerals (olivine, plagioclase, pyroxene, Cr-spinel, and (Ti-) magnetite) to shed light into the processes that led to the chemical evolution of the eruptive products. Our sample set includes the early tephra from the first weeks/months and the whole sequence of lava flows that followed. The mineral assemblage, texture, and chemical composition show a systematic evolution between the products from the opening of the explosive vent to the effusive stage. The early tephra are basaltic andesites with oscillatory-zoned olivine and plagioclase, zoned Cr-spinel, and rare pyroxene xenocrysts. In contrast, later erupted tephra and post-January 1944 lavas are basaltic andesites and andesites with normally-zoned olivine, Cr-spinel inclusions in equilibrium with the host olivine, and frequent orthopyroxene (after December 1947) with minor chemical zoning. The mineral chemistry data and the olivine diffusion timescales, together with whole rock geochemistry, suggest a convective magma regime with large temperature and oxygen fugacity gradients characterized by short timescales (few days) during the opening stage, followed by a steadier magma regime with longer timescales (few months) and including periodic magma recharge, mixing, and fractional crystallization. In addition, the mineralogical evidence we have gathered does not support considerable crustal assimilation at Paricutin. This study shows that monogenetic eruptions are far from being geochemically simple, and instead involve multiple magma batches with complex storage and mixing stages.

KEYWORDS:

Monogenetic volcanism; Crystal zoning; Diffusion timescales; Parícutin; Trans-Mexican Volcanic Belt

INTRODUCTION

Monogenetic eruptions are the most prevalent type of subaerial volcanism on Earth, occurring in intraplate, extensional, and subduction related settings (Cañón-Tapia, 2016). These eruptions are usually characterized by a small volume of mafic magma (<1 km^3; Kereszturi and Németh, 2012) emitted during a single episode of volcanic activity lasting from a few days to several years, and thus providing near-real time information on the physical and chemical characteristics of the ascending magma (e.g., Connor & Conway, 2000; Cañón-Tapia & Walker, 2004; Smith & Németh, 2017). Due to their relatively small size and low frequency of eruptions compared to polygenetic volcanoes, monogenetic centers are often perceived as low risk. However, our ability to forecast monogenetic volcanism is hazardously low, as eruptions tend to arise without compelling patterns in time and space within monogenetic volcanic fields, and geophysical warning systems typically lack a sufficient empirical record with which to compare real-time signals. It is therefore crucial to decipher source-to-surface magmatic pathways through geochemical studies on past volcanic products (Smith & Németh, 2017).

Traditionally, monogenetic eruptions were inferred to be fed from discrete batches of magma travelling rapidly through the crust, via simple conduit systems involving limited interactions (Smith & Nemeth, 2017). However, comprehensive studies of monogenetic eruptions based on whole rock major, trace element, and isotope geochemistry have increasingly revealed systematic changes in the composition of the magma with the eruption progress, which often correlate with changes in the volcano-stratigraphy (e.g., Brenna et al., 2010, 2011, 2012; McGee et al., 2012). These chemical variations have been attributed to a range of processes, including complex heterogeneous mantle melting and subsequent mixing of multiple magma batches, and/or variable degrees of fractionation and crustal assimilation (e.g., Reiners, 1998; Strong & Wolff, 2003; Cook et al., 2005; Haase & Renno, 2008; Smith et al., 2008; Brenna et al., 2010; 2011; Cebriá et al., 2011; McGee et al., 2011; 2012; Sohn et al., 2012; van Otterloo et al., 2014; Boyce et al., 2015), reigniting the debate on the origin and processes of monogenetic volcanism.

Despite the relatively small magnitude and short lifetime of individual monogenetic eruptions, their products often reveal complex pre-eruptive magma ascent histories (e.g., Jankovics et al., 2013; 2015; Albert et al., 2015; 2016; Re et al., 2017; Shane & Coote, 2018; Jankovics et al., 2019). Whole rock geochemistry can obscure primary magmatic processes since bulk samples represent a mixture of various melt and crystal compositions (e.g., Reubi & Blundy, 2009; Larrea et al., 2012; Ubide et al., 2014). Hybrid magmas can carry a history of crystallization over a range of pressure-temperature-composition paths, and contain an assortment of crystal populations including antecrysts, cogenetic phenocrysts, and recycled xenocrysts. In this regard, petrological studies using mineral zoning and textures offer an opportunity to address unanswered questions raised by whole rock geochemistry, including changes in the magmatic plumbing system with time, and the timescales of these processes (e.g., Costa et al., 2008; 2013; 2020; Davidson et al., 2007; Ginibre et al., 2007; Blundy & Cashman, 2008; Streck, 2008; Ubide & Kamber, 2018). Therefore, deciphering the magma source-to-surface path in monogenetic volcanoes requires whole rock geochemical studies combined with detailed mineral analyses, as we report in this study.

Paricutin is the youngest scoria cone in the Michoacán-Guanajuato volcanic field (Trans-Mexican Volcanic Belt; Fig.1A) with an exceptional exposure of continuous deposits from 1943-1952. The 9-year eruption was witnessed in its entirety from beginning to end (Luhr & Simkin, 1993, and references therein), and hence it is an ideal case study for integrating historical observations with whole rock and mineral chemistry of the complete eruptive sequence. This includes the first tephra ejected during the early explosive activity linked to the opening of the magmatic system (Albert et al., 2020), and the transition towards effusive activity with lava emissions, which characterized Paricutin's eruption until the cessation of volcanic activity. Our aim is to unravel the magmatic processes involved in the evolution of this historic monogenetic eruption and the role played by crustal contamination, which have certainly been controversial (e.g., Cebriá et al., 2011; Erlund et al., 2010; Johnson et al., 2010;

Larrea et el., 2019a; Luhr, 2001; McBirney et al., 1987; Rowe et al., 2011; Wilcox, 1954). We undertake a detailed examination of the petrology and chemistry of the rock-forming minerals and their variations with time. We use a subset of tephra and lava samples spanning the entire eruption to make inferences on the magma plumbing system dynamics, the magmatic processes controlling the evolution of the volcano, and their associated timescales.

PARICUTIN ERUPTION AND PREVIOUS STUDIES

Paricutin started erupting on the 20th of February 1943, and ended 9 years later on the 4th of March 1952 (Luhr & Simkin, 1993). The eruption was of great interest to the geological community worldwide because of the unique opportunity to witness and document the birth, development, decline, and cessation of activity of a small volcano (e.g., Segerstrom & Gutiérrez, 1947; Ordóñez, 1947; Wilcox & Gutiérrez, 1948; Segerstrom, 1950; Fries, 1953; Foshag & González-Reyna, 1956; Scandone, 1979; Yokoyama & de la Cruz-Reyna, 1990; Luhr & Simkin, 1993).

During the 9 years of the eruption, 23 lava flows were emplaced (Luhr & Simkin, 1993) covering 25 km^2 with an estimated total volume of ~1.6 km^3 (dense rock equivalent; Larrea et al., 2017). Most of the pyroclastic material was erupted during the first three years, extending over tens of km^2 forming a roughly circular deposit around the main cone, blanketing the pre-existing topography (Pioli et al., 2008). Notable characteristics of the Paricutin eruption include an erratic variation in effusion rate with an overall increase in the effective viscosity of the magma, a change in the importance of explosive relative to effusive activity, and in the bulk magma composition with time (Larrea et al., 2017). Previous studies dealing with the petrology and geochemical characteristics of lavas, tephra, and xenoliths found in lavas, together with melt inclusion studies, proposed that crustal contamination was an important process in the petrogenesis of Paricutin's magmas (e.g., Cebriá et al., 2011; Erlund et al., 2010; Johnson et al., 2010; Luhr, 2001; McBirney et al., 1987; Rowe et al., 2011; Wilcox, 1954). These studies led to the notion of Paricutin representing a classic example of assimilation-fractional crystallization

in a subduction calc-alkaline setting. However, the recent work on Os isotope systematics by Larrea et al (2019a) ruled out considerable crustal assimilation, and instead attributed the isotopic variations across the eruption to source heterogeneities. These authors proposed that primitive magma rises and mixes at mid-crustal depths with previously formed, slightly evolved melts, while the fractional crystallization process continues (i.e., magma recharge, mixing, and fractional crystallization). This model is consistent with a complex evolution involving multiple magma batches, as proposed by Rowe et al. (2011). In the present study, we use the Paricutin temporal-compositional sequence to characterize the petrology and mineral chemistry of tephra and lavas spanning the 9 years of eruption, which we use to make inferences on the magma plumbing system dynamics and the timescales of magmatic processes, and further explore the role of crustal contamination in Paricutin.

SAMPLES AND ANALYTICAL METHODS

Initial tephra deposits and subsequent fresh lava flows covering the entire time-span of the activity of the volcano were sampled and studied by Larrea et al. (2019a). A subset of these samples was selected for the current study, including four samples from the tephra fall in proximal areas erupted during the first weeks/months of explosive activity (T1: PAR-1537, T2: PAR-1536B, T3: PAR-1536E and T4: PAR-1209C; Fig. 1B), and a selection of seven lava flows (L) from the 23 eruptive phases (L3: PAR-1215, L7:PAR-1216; L14: PAR-1201, L17: PAR-1205, L20: PAR-1524, L22: PAR-1207 and L23: PAR-1520; Fig. 1B) (Luhr & Simkin, 1993). Sample location coordinates and whole rock analysis are reported in Larrea et al. (2019a).

A polarizing optical microscope and the JEOL JSM-7800F field emission scanning electron microscope at the Earth Observatory of Singapore, were used for petrographic analyses and to obtain backscattered electron (BSE) images, and quantitative chemical analyses of the minerals (see results in Tables I-V of the Electronic Appendix 1). Major element compositions of minerals from the lavas were obtained by electron probe micro-analysis (EPMA) using a

field emission gun JEOL JXA-8530F at Nanyang Technological University (Singapore), and a JEOL JXA-8200 at The University of Queensland Centre for Microscopy and Microanalysis (Australia). Mineral standards were used for calibration of both instruments and operating conditions were: 15 kV accelerating voltage, 15 to 25 nA beam current, a focused beam diameter of ca.1 μm, 20-30 s counting time on peak positions, and 5 s on background positions. ZAF was used for matrix correction. Core-to-rim traverses were performed on olivine, orthopyroxene, and feldspar macrocrysts with a spacing of 1-5 μm between analyses. Additional spot analyses were performed on all minerals. Major element compositions of the minerals from the T1-T4 tephra were published in Albert et al. (2020).

Electron backscattered diffraction (EBSD) patterns of olivine were obtained to determine the orientation of the crystallographic axes at the Nanyang Technological University, using a JEOL JSM-7800F field emission scanning electron microscope (SEM) equipped with an Oxford NordlysNano detector and Oxford's AZtec microanalysis software. We modelled diffusion of multiple elements in olivine (Fe, Mg, and Ni) from the lavas, representing maximum timescales due to potential diffusion modification during lava flow emplacement and cooling. The DIPRA software (Girona & Costa, 2013) was used to model the chemical profiles in olivine (n=13) to calculate the timescales and their uncertainties according to the relevant temperature, and oxygen fugacity. The results are reported in Table VI of the Electronic Appendix 1.

PETROLOGY AND WHOLE ROCK CHEMISTRY

The bulk composition of Paricutin eruption products changes with time, ranging from basaltic andesite to andesite (Fig. 2A). SiO_2 contents vary between 53.0 and 60.5 wt %, MgO from 3.5 to 7.5 wt %, with relatively low contents of Ni (43-180 ppm) and Cr (70-244 ppm). Tephra and lava flows exhibit typical arc geochemical signatures with an almost continuous compositional trend in Harker diagrams, although there is a change in slope at ~56 wt % SiO_2 for most oxides and trace elements (Fig. 2C-D). Overall the Mg# [Mg/(Mg+Fe^T) atomic ratio, where Fe^T

expresses total iron] decreases with eruption time, yet there are several periods where a reversal (increase in Mg#) is observed (Fig. 2B). Larrea et al (2019a) attributed these variations to magma recharge, mixing, and fractional crystallization, the main magmatic processes controlling the evolution of Paricutin magmas.

The petrography of Paricutin lavas was first described by Wilcox (1954), and later complemented by Bannister et al. (1998), who focused on Cr-spinels. Tephra and lava samples have microporphyritic textures characterized by small macrocrysts (200 μm-3.5 mm) embedded in a holocrystalline to hypocrystalline groundmass (Fig. 3). In this study, we use the term macrocryst for crystals >200 μm and microcryst for those <200 μm. The macrocryst content varies from about 20 vol. % in the early tephra T1 to <10 vol. % in tephra T4, accompanied by a progressive increase in crystal size (Fig. 3A-B). The lavas are characterized by a crystal content <8 vol. % and a progressive decrease in crystal size (Fig. 3C-F).

In addition, the macrocryst assemblage and modes, mineral textures, and compositions change with time (Fig. 4-5). Early tephra T1-T2 are characterized by olivine and feldspar macrocrysts, with rare orthopyroxene and clinopyroxene macrocrysts (Fig. 3A and 4). Tephra T3-T4 and all lavas are characterized by olivine and the absence of feldspar macrocrysts (except from isolated crystals; Fig. 3B-F and 4). The olivine macrocrysts are mantled by discontinuous orthopyroxene rims in L3 (also described by Wilcox (1954) in the 1943 and early 1944 lavas), and the olivine macrocrysts in the subsequent lavas through the end of the eruption are mantled by continuous orthopyroxene rims (Fig. 4C). Orthopyroxene macrocrysts occur after 1947 (whole rock SiO_2 >58 wt %), when olivine macrocrysts progressively decrease in abundance, towards the end of the eruption (Fig. 3E-F, 4 and 5). Cr-spinel crystals are present as inclusions in most olivine and orthopyroxene macrocrysts and, to a lesser extent, in the feldspar and scarce clinopyroxene macrocrysts (Fig. 3 and 4). The groundmass is composed of microcrysts of feldspar, olivine, orthopyroxene, clinopyroxene, (Ti-) magnetite, and minor glass (Fig. 3 and 4).

Xenoliths were described in detail by Wilcox (1954), and were observed in bombs erupted during the first years of explosive activity and hosted in lavas erupted in the first three years of effusive activity (McBirney et al., 1987). They are fragments of silicic intrusives (granite, granodiorite, and quartz monzonite) with a wide range of alteration, mostly composed of orthoclase and albitic plagioclase, opaque minerals, and accessory minerals (sphene, zircon, and apatite). Fourteen xenoliths collected from lavas erupted in the first years of activity were provided by the Smithsonian Museum of Natural History, but unfortunately, they were mostly received as powders or with a high degree of weathering, making petrographic determinations impossible. These samples were used for whole rock geochemical analysis (Larrea et al., 2019a).

MINERAL CHEMISTRY

In addition to the tephra mineral analyses reported in Albert et al. (2020) a selection of macrocrysts and microcrysts from each mineral was analyzed in selected lavas and tephras. Major element compositions of core-to-rim crystal traverses and individual spot analyses were determined by electron microprobe, and the complete dataset is reported in Tables I-V of the Electronic Appendix 1. In total, 130 olivine (including 55 core-to-rim profiles), 59 orthopyroxene (including 11 core-to-rim profiles), 6 clinopyroxene (including 2 core-to-rim profiles), 79 feldspar (including 11 core-to-rim profiles), and 131 spinel crystals were analyzed (see details in Electronic Appendix 2). Due to the differences in modal mineralogy, chemistry, zoning, and textures of the early tephra T1-T2 compared to tephra T3-T4 and lavas, these two groups are described separately below (Fig.4 and 5).

Olivine

Early tephra T1-T2 are characterized by subhedral to euhedral skeletal olivine macrocrysts with complex zoning (Fig. 4A-B). Multiple variations in forsterite occur along a single traverse with sharp changes (up to 10 mol% Fo# = 100 x Mg/[Mg+Fe] in less than 50 μm; Electronic Appendix 2). Olivine macrocrysts in T1-T2 have higher Fo#, CaO and NiO, and lower MnO

than in tephra T3-T4 and lavas (Fig. 5A and Electronic Appendix 2). Macrocryst cores in tephra T1-T2 are characterized by $Fo\#_{77-86}$, 0.11-0.22 wt % CaO, 0.04-0.48 wt % NiO, and 0.17-0.39 wt % MnO contents, whereas the rims show $Fo\#_{76-84}$, 0.13-0.37 wt % CaO, 0.02-0.23 wt % NiO, and 0.22-0.38 wt % MnO variations; microcrysts are characterized by $Fo\#_{72-81}$, 0.19-0.26 wt % CaO, 0.02-0.18 wt % NiO, and 0.25-0.54 wt % MnO contents (Fig. 5A and Electronic Appendix 2).

These olivine macrocrysts with complex zonation are progressively less abundant during the eruption sequence, and are substituted in tephra T3-T4 and lavas by subhedral to euhedral and minor skeletal, normally zoned macrocrysts with homogeneous wide cores ($Fo\#_{69-84}$, CaO: 0.08-0.25 wt %, NiO: 0.06-0.44 wt %, and MnO: 0.19-0.45 wt %) and more evolved rims ($Fo\#_{52-82}$, CaO: 0.10-0.35 wt %, NiO: 0.02-0.35 wt %, and MnO: 0.23-0.70 wt %; Fig. 4C-D and 5A and Electronic Appendix 2). The compositional change from the core to the rim (width <50 μm) is usually sharp, and therefore defined as single step zoning. In general, these weakly zoned olivine cores change to more evolved compositions as the eruption progresses, decreasing in Fo#-NiO and increasing in CaO-MnO with time (Fig. 5A and Electronic Appendix 2). However, the olivine compositions also follow whole rock Mg# reversals (Fig. 2B). For example, olivine macrocrysts from L3 are more evolved than those in L7, and macrocrysts from L20 are more evolved than those from L22 and L23 (Fig. 5A). The presence of orthopyroxene rims (5-20 μm) surrounding olivine macrocrysts is a distinctive characteristic, which appears for the first time as a discontinuous rim in L3, and continues through the end of the eruption as continuous rims (Fig. 4C). Moreover, the olivine macrocrysts from L4 and L14 are characterized by the presence of symplectitic outer rims of orthopyroxene and opaque minerals (see textural details in Fig. 4D). Olivine microcrysts in L3 have Fo_{60-74} compositions equivalent to the rims of the macrocrysts (Fig. 5A and Electronic Appendix 2).

Pyroxene

Four pyroxene macrocrysts were found in the early tephra T1 (Fig. 4E-F): one orthopyroxene (Wo_{3-3} En_{74-67} Fs_{22-30}) and three clinopyroxene crystals (Wo_{40-43} En_{47-40} Fs_{12-17}). Core-to-rim compositional profiles are provided in Electronic Appendix 2. The orthopyroxene displays an evolved, weakly zoned core characterized by Mg#= 70-72 (Mg#= 100xMg/[Mg+Fe^2] atomic ratio) and a more primitive rim (Mg#= 75-78 wt %; Fig. 4E and 5B), and is the most evolved orthopyroxene composition found in any of the eruption products. The three only clinopyroxene macrocrysts from the Paricutin sequence are in this unit, and they are oscillatory zoned (Mg#= 71-80 calculated as 100xMg/(Mg+Fe^{2+}+Fe^{3+}) atomic ratio; Fig. 4F and 5C) within a glomeroporphyritic assemblage with plagioclase. Some orthopyroxene (Wo_4 En_{73} Fs_{24}) and clinopyroxene (Wo_{27-35} En_{49-48} Fs_{24-16}) microcrysts from the tephra groundmass were also analyzed; the orthopyroxene microcrysts (Mg#= 76-77) are equivalent to the orthopyroxene macrocryst rims (Fig. 5B and Electronic Appendix 2). An analysis of a clinopyroxene microcryst in L3 returned a more evolved composition than the tephra microcryst value (Fig. 5C).

Orthopyroxene macrocrysts are absent in the rest of the tephra and lavas from 1943 until November 1947. The first re-appearance of orthopyroxene as macrocrysts is in L14, becoming a ubiquitous macrocryst (Wo_{2-3} En_{80-70} Fs_{18-27}) that coexists with olivine until the end of the eruption in March 1952 (Fig. 5). These orthopyroxene macrocrysts show mild normal and oscillatory zoning, and occur as glomerocrysts and/or as isolated crystals (Fig. 4G-H). Core-to-rim compositional profiles are provided in Electronic Appendix 2. Three main groups can be identified: 1) macrocrysts with normal zoning, 2) macrocrysts with primitive cores that evolved and later developed primitive rims (Fig. 4H), and 3) macrocrysts with evolved cores surrounded by primitive shoulders and oscillatory outer rims (Fig. 4G). Despite the existence of these groups, the compositions of the crystals from the different lava flows overlap and define a constrained evolutionary trend with Mg#= 73-86 , 52.6-56.8 wt % SiO_2, 0.79-4.6 wt % Al_2O_3, 0.11-0.35 wt % TiO_2, and 0.01-0.76 wt % Cr_2O_3 (Fig. 5B and Electronic Appendix 2).

Microcrysts of orthopyroxene (Wo_{2-7} En_{79-68} Fs_{18-25}) and clinopyroxene (Wo_{35} En_{42} Fs_{23}) show normal zoning and define a trend towards more evolved compositions compared to the macrocrysts in most major elements (Electronic Appendix 2). Orthopyroxene crystals forming outer rims (5-20 μm) around olivine macrocrysts (Fig. 4C) are compositionally equivalent to the orthopyroxene macrocryst rims analyzed in the same sample (L17; Mg#= 73-75 and Wo_{3-7} En_{72-68} Fs_{25-25}; Fig. 5B and Electronic Appendix 2).

Feldspar

Feldspar macrocrysts are mostly present in the early tephra T1-T2 (Fig. 4I); they display subhedral and skeletal textures and oscillatory zoning, ranging from bytownite to labradorite (An_{78-52} Ab_{22-46} Or_{0-2}), whereas the microcrysts are mostly labradorite (An_{68-47} Ab_{32-49} Or_{0-4}) (Fig. 5D and Electronic Appendix 2). Five macrocrysts have been found in the lava flows and they appear as spongy-textured isolated macrocrysts (Fig. 4K), ranging from bytownite to labradorite (An_{81-59} Ab_{19-39} Or_{0-1}; Fig. 5D and Electronic Appendix 2). Microcrysts range from labradorite to andesine (An_{62-44} Ab_{37-53} $Or_{1-2;}$ Fig. 5D and Electronic Appendix 2) with compositions equivalent to the rim of the macrocrysts.

Spinel

Spinel microcrysts occur as inclusions in macrocrysts and in the rock groundmass, in tephra and lavas spanning the entire Paricutin eruption. Spinel crystals hosted in macrocrysts are small (4-30 μm) euhedral to subhedral isolated crystals, clusters of crystals, and chains (Fig. 3 and 4). They have been analyzed as inclusions in olivine macrocrysts from tephra and lavas (Fig. 4J and 4L), and in a clinopyroxene macrocryst from the early tephra T1 (Fig. 4F). The spinel crystals hosted in olivine macrocrysts from the tephra and lavas are Cr-spinel, with an increase in Cr# [Cr/(Cr+Al) atomic ratio] (0.44-0.79), Fe^{3+}# [Fe^{3+}/(Fe^{3+}+Cr+Al) atomic ratio] (0.12-0.50), and TiO_2 (0.55-7.43 wt %) coupled with a decrease in Mg# [Mg/(Mg+Fe^{2+}) atomic ratio] (0.59-0.19) as the eruption progressed (Fig. 5E and Electronic Appendix 2). Some of the Cr-spinel crystals hosted in the olivine macrocrysts with complex zonation from the early tephra T1 are

chemically zoned despite their small size, and occur across the core, outer margin and/or rim of the olivine macrocrysts (Fig. 4J). The cores of the zoned Cr-spinel crystals within the early tephra T1 (Cr#= 0.44-0.51, Mg#= 0.59-0.47, Fe^{3+}#= 0.12-0.20, TiO_2= 0.55-0.96 wt %) follow the trend defined by the Cr-spinel crystals hosted in olivine macrocrysts from the lavas; however, the outer rims have a distinct composition with similar Cr# (0.43-0.49), higher Fe^{3+}# (0.30-0.33) and TiO_2 (1.93-3.72 wt %), and lower Mg# (0.44-0.37) than their respective cores (Fig. 5E and Electronic Appendix 2). In contrast, the spinel hosted in the clinopyroxene macrocryst (Fig. 4F) from the early tephra is a Ti-magnetite with Cr#= 0.03, Mg#= 0.20, Fe^{3+}#= 0.86-0.87, and TiO_2= 8.68-9.06 wt % (Fig. 5E and Electronic Appendix 2).

Spinel microcrysts within the groundmass are frequently larger (18-40 μm) than those hosted in the macrocrysts. They are classified as Ti-magnetite and magnetite with a Cr#= 0.03-0.79, Mg#= 0.25-0.02, Fe^{3+}#= 0.39-0.97, and TiO_2= 3.25-15.61 wt % (Fig. 5E and Electronic Appendix 2). The composition of the Ti-magnetite and magnetite groundmass microcrysts follows the same linear trend as the Cr-spinel crystals hosted in olivine and clinopyroxene, defining an increase of Fe^{3+}# accompanied by an increase of TiO_2 content with time (Electronic Appendix 2). The small size of opaque minerals forming the symplectitic outer rims of olivine macrocrysts from L4 and L14 (Fig. 4D) precluded in situ analysis.

DISCUSSION

Origin of crystal populations and potential links with crustal assimilation

Paricutin macrocrysts vary in content, texture, and composition with time, defining crystal populations that can be exploited to obtain insight into the processes, depths and timescales that govern magma storage prior to eruption (e.g., Kahl et al., 2015; Pankhurst et al., 2018; Ubide et al., 2014). The macrocrysts could potentially be classified as phenocrysts, antecrysts, or xenocrysts, depending on whether or not they are cogenetic with the host melt (e.g., Davidson et al., 2007; Ginibre et al., 2007; Jerram & Martin, 2008; Larrea et al., 2012; Pankhurst et al., 2018; Ubide et al., 2014). Here, crystal-melt Fe-Mg equilibrium diagrams ($Kd^{Mineral/Melt}$ =

$(X_{Fe}/X_{Mg})^{Mineral}$ / $(X_{Fe}/X_{Mg})^{Melt}$; Fig. 6) are used to decipher the origin of the different crystal populations. We approximate melt compositions via whole rock data, since the samples have low crystal content. Similarly, spinel-olivine equilibrium diagrams (Fig. 6D) based on the Fe^{2+}-Mg exchange between spinel and olivine are useful to estimate the Fo# content of the olivine coexisting with spinel at constant temperature (Dick & Bullen, 1984 and references therein). We apply these equilibrium tests below.

Olivine

To test for olivine-melt equilibrium, we used the Fe–Mg exchange distribution coefficient (Kd) value for Paricutin melts of 0.34±0.02 calculated by Erlund et al. (2010) following the method of Toplis (2005), which includes the effects of temperature, pressure, melt composition, and dissolved H_2O content. As observed in Fig. 6A, some macrocryst compositions in each analyzed sample fall within the equilibrium range, whereas most of the compositional variation falls below. Those compositions within the equilibrium field should be the only ones interpreted as cogenetic phenocrysts in equilibrium with the rock in which they are hosted; therefore, it is crucial to link the observed equilibrium compositions with the olivine macrocryst zoning in early tephra T1-T2 vs. tephra T3-T4 and lavas. In the tephra T3-T4 and lavas (see L20 inset in Fig. 6A), the homogeneous compositions of the wide cores are in equilibrium with their host whole rock melts, whereas the rims and the microcryst compositions fall below the equilibrium curve owing to crystallization upon ascent, eruption and cooling at the surface (progressive fractionation/crystallization). This observation holds even considering the whole rock Mg# reversals throughout the eruption (Fig. 2B). In contrast, the skeletal olivine macrocrysts in T1-T2 are characterized by alternating, large and sharp compositional variations (complex zoning), and only certain sections of the compositional profile seem to fall within the equilibrium range with the host-melt (see T2 inset in Fig. 6A and the core-to-rim profiles in Electronic Appendix 2). Classic magma mixing (i.e., new magma intrusion in a compositionally different magma reservoir) is unlikely responsible for the recorded complex zoning, since there are no clusters of olivine core, mantle, or rim compositions that could be indicative of distinct magma batches and

reservoirs. Instead, Albert et al. (2020) proposed that large and rapid changes in temperature and fO_2 are needed to explain the zoning of olivine macrocrysts in the early tephra T1-T2 where early olivine crystals grew rapidly (outside equilibrium) during conduit opening and magma transport to the surface.

Pyroxenes

Clinopyroxene macrocrysts were only found in the early tephra T1 (Fig. 4F), and are relatively evolved (Mg#= 71-80). According to clinopyroxene-melt Fe-Mg equilibrium exchange (Kd= 0.28 ± 0.08; Putirka, 2008; Fig. 6B), these compositions are too evolved to have crystallized from the melt represented by whole rock T1 (Mg#= 64). Accordingly, these clinopyroxene macrocrysts are xenocrysts from a magma that is more evolved (Mg# ~ 52) than any Paricutin product.

Orthopyroxene macrocrysts are significantly more abundant than clinopyroxenes, although there is a noticeable difference between the orthopyroxene of the early tephra T1, and the macrocrysts in the lavas after December 1947 (Fig. 4 and 5B). Orthopyroxene-melt equilibrium (Kd= 0.29 ± 0.06; Putirka, 2008) shows that the orthopyroxene macrocrysts found in early tephra T1 are clearly out of equilibrium (Fig. 6C), indicating their xenocrystic origin, similar to the clinopyroxene xenocrysts found in the same early tephra.

The occurrence of low-Mg# clino- and orthopyroxene xenocrysts could potentially suggest assimilation of crustal materials (e.g., granitic xenoliths), however, their occurrence in the early tephra T1 and absence within the rest of the eruptive sequence argues against significant crustal assimilation, and points to their presence as crustal fragments ripped off during the violent opening of the system. In contrast, lava-hosted orthopyroxene macrocrysts and microcrysts plot within or below equilibrium with the host melt (Fig. 6). Thus, the orthopyroxene macrocrysts can be classified as: 1) phenocrysts with irregular cores and normal zoning (L20: PAR-1524 Opx5-A inset in Fig. 6C), 2) antecrysts with primitive cores formed

from more primitive magmas, later recycled by co-magmatic melts (L17: PAR-1205 Opx1-A inset in Fig. 6C), and 3) antecrysts with evolved cores formed from more evolved magmas, later incorporated and overgrown in equilibrium by successive Paricutin magmas (L23: PAR-1520 Opx2-A inset in Fig. 6C). The last two groups highlight the relevance of mafic recharge events, consistent with the whole rock reversals in Mg# (Fig. 2B). Lava-hosted clinopyroxene and orthopyroxene microcrysts, as well as olivine microcrysts, fall far below the equilibrium curves (Fig. 6B-C) owing to progressive fractional crystallization of the melts in which they formed.

Orthopyroxene rims (5-20 μm) around olivine macrocrysts (Fig. 4C) are equivalent in composition to the microcrysts and the orthopyroxene macrocryst rims of the same sample (see L17 triangles in Fig. 6C). These are likely orthopyroxene peritectic rims, that together with the symplectitic rims (Fig. 4C-D), formed during slow cooling and increase of silica activity of the magma (forsterite+silica → enstatite; Zellmer et al., 2016) during eruption and emplacement. The lack of these rims in the tephra may reflect the quick quenching of the tephra relative to lavas, and/or that olivines did not reach the peritectic reaction due to the primitive composition of the early melts.

Plagioclase

Plagioclase macrocrysts and microcrysts in the early tephra are texturally different from those in the lavas (Fig. 4). Plagioclase macrocrysts in the early tephra are subhedral and skeletal, with oscillatory zoning and a continuous compositional variation toward the composition of the microcrysts, which indicates their likely genetic relationship by fractionation. The complexity of the An zoning resembles that of the Fo# olivine macrocrysts in the early tephra (see above), probably recording the same disequilibrium conditions and fast growth during conduit opening and magma transport to the surface (Albert et al., 2020). The presence of plagioclase phenocrysts in the early tephra, and in the 1943 and early 1944 lavas reported by Wilcox (1954) and McBirney et al. (1987) (samples not available for this study), suggests that water content was relatively low in the initial magmas, as demonstrated in experimental studies of calc-

alkaline magma differentiation (e.g., Eggler, 1972; Blatter & Carmichael, 1998; Moore & Carmichael, 1998; Carmichael, 2002; Grove et al., 2003). In contrast, the lack of plagioclase macrocrysts in the lavas is likely due to the greater water content of the magmas at depth (>2.5 wt % H_2O; Larrea et al., 2019a), whereas microcryst growth was related to efficient degassing of the magmas during ascent and extrusion.

The scarce spongy-textured plagioclase macrocrysts (<1 vol. %), which could preliminarily be considered as remnants of assimilated xenolith material due to their texture, are more anorthite-rich (An_{81-59}) than any other plagioclase feldspar found, including those in the more primitive products from Paricutin (L20 in Fig. 5D). The rims of these macrocrysts have the same composition as the microcrysts forming the groundmass. Thus, the plagioclase macrocrysts found in the lavas are probably antecrysts formed in more primitive and/or water-rich melts than those erupted at Paricutin.

Spinel

Cr-spinel inclusions in olivine and orthopyroxene are ubiquitous across the Paricutin sequence. Their presence, despite the low Cr content of the rock (<250 ppm), suggests that water dissolved in the melt lowered the liquidus temperature of silicates (e.g., orthopyroxene) such that Cr-spinel was the first phase to crystallize (Bannister et al., 1998). This further explains the lack of orthopyroxene macrocrysts until December 1947, when the melts became more evolved.

The cores of Cr-spinel crystals included in olivine macrocrysts from tephra and lavas show a well-defined evolutionary trend in Cr#-Mg#-Fe^{3+}# ratios and TiO_2 contents as the eruption progressed (Electronic Appendix 2). We tested whether the Cr-spinel was in equilibrium with the host olivine using Cr# vs. Mg# diagrams at 1200 °C (Figure 6D; Dick & Bullen, 1984). Overall, Cr-spinel inclusions are in equilibrium with Fo_{71-87}, in accordance with the Fo# contents of their host. However, the zoned Cr-spinel crystals (i.e., outer rims) within the olivine macrocrysts with complex zonation from the early tephra T1 suggest more complex

processes. These may record changes in temperature, oxygen fugacity, and volatile pressure which led to subsequent growth of Ti-rich spinel outer rims (e.g., Morgado et al., 2019; Albert et al., 2020). In contrast, the (Ti-) magnetite microcrysts within the groundmass from all eruptive products and those hosted in clinopyroxene plot mostly below Fo_{70}, following an evolutionary trend of coeval Fe^{3+}# and TiO_2 increase (Electronic Appendix 2). This trend can be explained by fractional crystallization, because the composition of the (Ti-) magnetite microcrysts evolves towards higher Fe^{3+}# and TiO_2 contents with the composition of the rock in which they are included. The evolved compositions of the Ti-magnetite microcrysts (diamond in Fig. 6D and Electronic Appendix 2) hosted in the clinopyroxene macrocryst from the early tephra T1 are also in agreement with the xenocrystic origin attributed to this clinopyroxene.

The Paricutin petrological characterization of the minerals with eruptive sequence shows a wide variability of mineral textures and compositions, the existence of phenocrysts, antecrysts, and scarce xenocrysts with large differences between the early tephra and the lavas. In addition, we find little petrographic evidence of contamination of the Paricutin magmas by the xenoliths studied by Wilcox (1954). Some of the crustal wall-rocks were incorporated during the conduit opening, as shown by the occurrence of silicic intrusives hosted in bombs and lavas erupted during the first three years described by McBirney et al. (1987); but we did not find abundant xenocryst or resorbed crystal cargoes with compositions that could be attributed to these silicic intrusives. Instead, only some rare pyroxene xenocrysts were observed in the early tephra T1. In addition, we did not find xenoliths in our multiple scouting fieldwork campaigns around the lava outcrops. Therefore, the Paricutin mineral cargo, together with the whole rock multi-isotopic study by Larrea et al. (2019a), are inconsistent with the previously suggested significant crustal assimilation by Paricutin magmas.

Thermobarometry

Orthopyroxene macrocryst compositions from L14-L23 were used to explore pressure and temperature crystallization conditions using mineral-melt calibrations by Putirka (2008). Each

macrocryst composition was paired with the corresponding host whole rock (Fig. 6C), and only those in equilibrium are reported in Table II of the Electronic Appendix 1. The water content in the melt was considered to be 3 wt % H_2O, in accordance with estimates from olivine-hosted glass/melt inclusions in lavas (1.8–4.2 wt %; Erlund et al., 2010; Luhr, 2001). We report thermobarometric results (Fig. 7) from Eq. 28a thermometer (±28 ºC) and Eq. 29a barometer (±210 MPa) of Putirka (2008). Macrocrysts define a polybaric crystallization trend between 1042-1120 ºC and 0-800 MPa that is remarkably constant throughout the eruption (see kernel density estimation in Fig. 7), indicating repetitive decompression paths across the lifetime of the volcano.

Larrea et al. (2019a) proposed that Paricutin magmas can be reproduced by polybaric differentiation (from 1176 ºC and 300 MPa to 950 ºC and 100 MPa) that includes recharge+mixing+fractionation of olivine, spinel, orthopyroxene, clinopyroxene, feldspar, and minor Ti-magnetite. The reversals in Mg# of the whole rock with time (Fig. 2B) were reproduced by Larrea et al (2019a) using the Magma Chamber Simulator (MCS; Bohrson et al., 2014), and an open-system magma evolution of primitive magma replenishment during cooling and crystallization. This proposed scenario agrees with the range of temperatures and pressures estimated for the orthopyroxene macrocrysts in this study, and with the pressures of entrapment of 245 to 100 MPa calculated by Luhr (2001) from olivine-hosted melt inclusions, which may return lower pressures than mineral-melt barometers due to decrepitation issues (Maclennan, 2017; Venugopal et al., 2020). Therefore, the whole rock variations of Paricutin magmas, their mineral textures and compositions (see discussion above), and the thermobarometric estimations are all in agreement with the occurrence of repetitive magma recharge+mixing+fractionation events with time.

Olivine diffusion timescales

The homogeneous cores of the olivine macrocrysts in the lavas seem to be in equilibrium with their host rock and therefore, they classify as phenocrysts (Fig. 6A). This implies that the small

amount of olivine (<8 vol. %) was formed in all cases after mixing, i.e., following "real time" fractionation. We acknowledge that these olivine crystals could have crystallized much earlier and experience different thermal events that could have been effectively reset by diffusion (i.e., recycled antecrysts). We cannot distinguish between these possibilities, but olivine Mg# contents are in agreement with repetitive magma recharge events during the nine years of eruption.

The normally zoned olivine phenocrysts from the lavas were selected to calculate the maximum time elapsed between the arrival of a new batch of melt and the eruption. Thirteen compositional profiles in olivine phenocrysts from L3, L7, L20, and L23 lavas were modelled. Olivine phenocrysts from L3 and L7 have Fo# cores between 80 and 82 and display normal Fo zoning, whereas NiO (wt %) profiles show some minor compositional variations along the traverse (Fig. 8A; see details in Electronic Appendix 3). Olivine phenocrysts from L20 and L23 have Fo# core values between 78 and 80 and are also normally zoned, whereas NiO (wt %) mainly displays flat patterns or slight normal zoning (Fig. 8A; see details in Electronic Appendix 3).

The Fe-Mg and Ni diffusion between cores and rims were modelled using the DIPRA software (Girona & Costa, 2013) and corrected for crystal orientation and diffusion anisotropy, considering the core plateau at a given concentration of Fo# and the observed composition at the rim reflecting the initial conditions (Fig. 8A; see all parameters used in Table VI of the Electronic Appendix 1). In three olivine phenocrysts from L3 (1215-2, 1215-3 and 1215-10) some analyzed points at the rim were discarded since the last part of the compositional profile has a different slope and could be related to late-stage crystallization (e.g., Albert et al., 2015; see Electronic Appendix 3). The oxygen fugacity (QFM+1) and temperature were chosen in accordance with the Rhyolite-MELTS model proposed by Larrea et al. (2019a). For olivine phenocrysts from L3 and L7 (whole rock MgO ~5.5 wt %) we used a temperature of 1100±20 °C, and for olivine phenocrysts from L20 and L23 (whole rock MgO ~3.6 wt %) we used

1040±20 °C. Our calculations show similar timescales for the four lava flows (Fig. 8; Table 1), mainly between 30 and 300 days. In some olivine phenocrysts from L3 and L7, modelling of Fo# and Ni returned somewhat different timescales (Fig. 8B; see Electronic Appendix 3). This could be due to the fact that the NiO diffusion coefficient was determined for higher Fo# values than the ones studied here (85-90; Petry et al., 2004) or to a growth component for the zoning, with different effects on NiO and Fo# (e.g., Costa et al., 2008, 2020).

Figure 9 shows the calculated timescales for each olivine phenocryst from lava flows plotted against the eruption month. For all the samples where we undertook diffusion chronometry, timescale results are similar (Fig. 8B and 9). This fact is in agreement with repetitive magma recharges (multiple magma batches) across the lifetime of the volcano, as previously proposed by Larrea et al. (2019a) and Rowe et al. (2011) and outlined in Fig. 2B.In contrast, olivine phenocrysts in the early tephra with complex zoning patterns (Electronic Appendix 2), show Fo# patterns that are broadly a mirror image of the NiO wt % contents, but the NiO profiles are sharper than those of Fo#. Albert et al. (2020) obtained ascent rates of one to ten days for early tephra T1-T2 olivines, and longer timescales (one day to about a month) for olivine macrocrysts within tephra T3-T4, suggesting that growth was a main contribution to these cyclic compositional variations.

The evolution of olivine compositional profiles from the early tephra to the lavas together with the textural evolution of the olivine phenocrysts from skeletal (fast growth) to subhedral-euhedral (slow growth), suggests that the growth rate progressively decreased, and the shape of compositional profiles became more strongly controlled by diffusion over growth, as the eruption progressed. In this regard, the short timescales obtained from the early tephra are related to the system opening stage, whereas the longer timescales from the later tephra and lavas account for the repetitive magma recharge and mixing processes that occurred during the Paricutin eruption.

Nine-year evolution of the plumbing system

After 45 days of precursory seismicity, the eruption started on the 20th of February 1943 with continuous pyroclastic material ejected from the first fissure vent, allowing rapid growth of the cone (Foshag & González-Reyna, 1956; Yokoyama & de la Cruz-Reyna, 1990; Luhr & Simkin, 1993). The emission of the first lava flow occurred the second day after initiation of the eruption from the newly formed 50-m-high horseshoe-shaped scoria cone (Ordóñez, 1947). This "system opening" stage mainly comprised the early explosive activity (T1-T2) and the intermittent effusive activity (samples not available for this study), characterized as basaltic andesites with a complex suite of crystals (Fig. 10A). The pre-eruptive magma volatile contents and degassing mechanisms were proposed as key factors controlling the explosive activity at Paricutin (Larrea et al., 2017). The complex crystal zoning patterns recorded by olivine and plagioclase phenocrysts, and Cr-spinel microcrysts from these first explosive products (Fig. 4), likely record an early process of dike propagation and the opening of a new volcanic conduit that involved large and localized changes in magma composition due to rapid changes in temperature and fO_2 (Albert et al., 2020). During this initial violent vent opening event, a set of evolved pyroxene and Ti-magnetite xenocrysts (Fig. 4) and granitic xenoliths (McBirney et al., 1987) from the crust were ripped off the conduit walls and brought up to the surface. The duration of this opening event is unknown, but it is likely on the order of weeks/months, as complex mineral zoning and xenocrysts are only recognized in the tephra fall deposits collected 125 cm above the paleosol (Larrea et al., 2019a) and in the 1943 and early 1944 lava ejecta according to petrographic descriptions by Wilcox (1954) and McBirney et al. (1987). These results agree with timescales of less than one month obtained for the early tephra by Albert et al. (2020).

After this short "system opening" stage, the rest of the eruption was mostly dominated by irregular, short-lived eruptions of lava flows interrupted by episodic Vulcanian explosions. This "steady-state" stage comprises the rest of the tephra (T3-T4) and lavas erupted from January 1944 through the end of the eruption in March 1952 (L3-L23). These eruptive products evolved from basaltic andesites to andesites and are characterized by normally zoned olivine,

Cr-spinel in equilibrium with its host olivine, and frequent orthopyroxene with minor chemical zoning (after 1947). Together, whole rock geochemistry (Larrea et al., 2019a) and mineral data (this work) support a model in which magma fractionation, intermittently reversed by subtle magma recharge events with melts of similar compositions, controlled the evolution of Paricutin magmas in this "steady-state" stage. In this model, Paricutin magmas formed by heterogenous melting of a mantle source over time at pressures of ~1.3–1.6 GPa, and such primitive magmas rose and mixed at mid-crustal depths (<300 MPa) with previously formed, slightly more evolved melts, while the fractional crystallization process continued (Fig. 10B). This scenario explains how Paricutin products and their minerals became generally more evolved through time, despite the existence of reversals in the Mg# content, as well as the coexistence of different crystal populations (i.e., phenocrysts, antecrysts, and xenocrysts) in the magmas. Furthermore, the scarcity of xenocrystic material in the mineral cargo lends further support to the hypothesis of limited to no crustal assimilation.

We interpret the change of mineral modes, the geochemical variations, and the timescales resolved through olivine profiles, as an early transition between two distinct eruptive regimes. Convective magma dynamics with large gradients in temperature and fO_2 during the dike injection and vent opening stage, changed within hours/days/months from eruption onset towards a more steady and stable magma flow enabled by periodic magma recharges that fueled volcanism for 9 years (Fig. 10).

Comparison with other monogenetic systems within the Michoacán-Guanajuato volcanic field

The Michoacán-Guanajuato volcanic field (MGVF) is the largest monogenetic field associated with a subduction zone on Earth (Valentine & Connor, 2015), comprising >1000 monogenetic centers over 40,000 km^2. The MGVF has been the subject of intense research (e.g., Hasenaka & Carmichael, 1985) due to its historical eruptions, but also because it is an aerially extensive field, which poses risks to important population centers. Volcanic fields generally display

changes in the style of eruptive activity throughout their life span (e.g., Smith & Németh, 2017), however recent volcanological studies of Holocene monogenetic clusters within the MGVF near the small cities of Tacámbaro (Mahgoub et al., 2017), Zacapu (Reyes-Guzmán et al., 2018; Mahgoub et al., 2018), and Tancítaro (Larrea et al., 2019b), have revealed that they erupted in a similar style and followed similar compositional trends. Each of these clusters started with Strombolian activity, initially building a basaltic andesite scoria cone followed by associated lava flows. Subsequently, several hundreds of years later, nearby vents erupted additional silicic andesite lava flows (Mahgoub et al., 2017; Reyes-Guzmán et al., 2018; Larrea et al., 2019b). Given the chemical similarities between Paricutin and the Tacámbaro, Zacapu, and Tancítaro clusters, we entertain the hypothesis that the evolution of crystal textures and zoning patterns with time could also apply to the latter. If so, the sequence of explosive opening linked to dike propagation and opening of a new volcanic conduit, followed by transitional magma dynamics to effusive outpouring as described here for Paricutin, could apply to other monogenetic centers/clusters in the area. This line of research of applying detailed mineral- and whole rock-scale approaches through time, is worth pursuing to contribute to a better understanding of the Mexican volcanic arc, and monogenetic volcanism and eruptive styles in general.

CONCLUSIONS

Our petrological study of the Paricutin eruptive sequence shows that monogenetic volcanoes can be far from simple in terms of their magmatic evolution and the range of magmatic processes operating throughout their eruption. Unique access to the very first eruptive products, often difficult to locate and/or access due to coverage by younger volcanic products, together with systematic sampling of the eruptive phases represented by the extensive lava flow field, allowed for an exhaustive investigation of the evolution of the volcanic plumbing system across the explosive and effusive eruptive phases. In addition, this detailed investigation illustrates the importance of integrating volcanological and geochemical data and combining whole rock geochemical studies with multi-mineral-scale analyses and timescales, to infer

temporal changes in magmatic processes and the configuration of the underlying plumbing system. The present study of Paricutin volcano is a good example of the success of this combined approach to clarify the processes that lead to a chemically zoned eruption, also revealing a compositional transition from explosive opening to effusive outpouring. The transition in eruptive style coupled with the change in olivine compositional profiles, which became more strongly controlled by diffusion over growth as the eruption progressed. A similar approach to volcanoes in other monogenetic fields should provide a better understanding of the processes and timescales involved in these eruptions and thus to a better mitigation of their hazards.

ACKNOWLEDGMENTS

We warmly thank Dr. Jason Herrin, Dr. Lilu Cheng, and Dr. Jeffrey Oalmann for help, advice and assistance during microprobe and SEM work at the Earth Observatory of Singapore, and Al-Tamini Tapu for microprobe work at The University of Queensland. We are grateful to Sergio Salinas and Dave Kuentz for help during fieldwork in Mexico. We kindly thank the Department of Mineral Sciences of the Smithsonian Institution for providing specimens from Paricutin. This work was supported by the National Science Foundation grant EAR 1019798 awarded to Prof. Elisabeth Widom. Dr. Patricia Larrea was supported by NSF EAR 1019798 (2014-2016) and a UNAM-DGAPA postdoctoral fellowship (2018-2019). Dr. Helena Albert and Prof. Fidel Costa were supported by a National Research Foundation Investigatorship Award (grant number NRF-NRFI2017-06) from Singapore. Dr. Helena Albert is currently a Serra Húnter Lecturer Professor at the University of Barcelona. Dr. Teresa Ubide was supported by The University of Queensland (grants UQECR1717581 and UQFREA2019001828). Dr. Vanessa Colás was supported by the research programs CONACYT-Ciencia Básica (A1-S-14574) and UNAM-PAPIIT (IA-101419 and IA-102121). Work by Dr. Claus Siebe was supported by Dirección General de Asuntos del Personal Académico through projects UNAM-DGAPA IN-103618 and IN-104221. Constructive reviews by T. Shea, two anonymous

reviewers, and editor G. Wörner are thankfully acknowledged and led to great improvement of the manuscript.

REFERENCES

Albert, H., Costa, F. & Martí, J. (2015). Timing of magmatic processes and unrest associated with mafic historical monogenetic eruptions in Tenerife Island. Journal of Petrology 56, 1945–1966.

Albert, H., Costa, F. & Martí, J. (2016). Years to weeks of seismic unrest and magmatic intrusions precede monogenetic eruptions. Geology 44, 211–214.

Albert, H., Larrea, P., Costa, F., Widom, E. & Siebe, C. (2020). Crystals reveal magma convection and melt transport in dyke-fed eruptions. Scientific Reports 10, 11632.

Bannister, V., Roeder, P., & Poustovetov, A. (1998). Chromite in the Paricutin lava flows (1943–1952). Journal of Volcanology and Geothermal Research 87(1-4), 151-171.

Blatter, D. L., & Carmichael, I. S. (1998). Plagioclase-free andesites from Zitacuaro (Michoacan), Mexico: petrology and experimental constraints. Contributions to Mineralogy and Petrology 132(2), 121-138.

Blundy, J., & Cashman, K. (2008). Petrologic reconstruction of magmatic system variables and processes. Reviews in Mineralogy and Geochemistry 69(1), 179-239.

Bohrson, W. A., Spera, F. J., Ghiorso, M. S., Brown, G. A., Creamer, J. B., & Mayfield, A. (2014). Thermodynamic model for energy-constrained open-system evolution of crustal magma bodies undergoing simultaneous recharge, assimilation and crystallization: the magma chamber simulator. Journal of Petrology 55(9), 1685–1717.

Boyce, J., Nicholls, I., Keays, R. & Hayman, P. (2015). Variation in parental magmas of Mt Rouse, a complex polymagmatic monogenetic volcano in the basaltic intraplate Newer Volcanics Province, southeast Australia. Contributions to Mineralogy and Petrology 169(2), 1-21.

Brenna, M., Cronin, S. J., Németh, K., Smith, I. E. M. & Sohn, Y. K. (2011). The influence of magma plumbing complexity on monogenetic eruptions, Jeju Island, Korea. Terra Nova 1-6.

Brenna, M., Cronin, S.J., Smith, I. E. M., Maas, R. & Sohn, Y. K. (2012). How small-volume basaltic magmatic systems develop: a case study from the Jeju Island Volcanic Field, Korea. Journal of Petrology 53, 985–1018.

Brenna, M., Cronin, S. J., Smith, I. E. M., Sohn, Y. K. & Németh, K. (2010). Mechanisms driving polymagmatic activity at a monogenetic volcano, Udo, Jeju Island, South Korea. Contributions to Mineralogy and Petrology 160(6), 931-950.

Brenna, M., Cronin, S. J., Smith, I. E., Tollan, P. M., Scott, J. M., Prior, D. J., Bambery, K. & Ukstins, I. A. (2018). Olivine xenocryst diffusion reveals rapid monogenetic basaltic magma ascent following complex storage at Pupuke Maar, Auckland Volcanic Field, New Zealand. Earth and Planetary Science Letters, 499, 13-22.

Cañón-Tapia, E. (2016). Reappraisal of the significance of volcanic fields. Journal of Volcanology and Geothermal Research 310, 26-38.

Cañón-Tapia, E. & Walker, G. P. (2004). Global aspects of volcanism: the perspectives of "plate tectonics" and "volcanic systems". Earth-Science Reviews 66(1-2), 163-182.

Carmichael, I. S. (2002). The andesite aqueduct: perspectives on the evolution of intermediate magmatism in west-central (105–99 W) Mexico. Contributions to Mineralogy and Petrology 143(6), 641-663.

Cebriá, J. M., Martiny, B. M., López-Ruiz, J., & Morán-Zenteno, D. J. (2011). The Parícutin calc-alkaline lavas: New geochemical and petrogenetic modelling constraints on the crustal assimilation process. Journal of Volcanology and Geothermal Research 201(1), 113-125.

Connor, C. B., Conway, F. M., & Sigurdsson, H. (2000). Basaltic volcanic fields. Encyclopedia of Volcanoes, Academic Press, 331-343.

Cook, C., Briggs, R. M., Smith, I. E. M. & Maas, R. (2005). Petrology and geochemistry of intraplate basalts in the South Auckland Volcanic Field, New Zealand: Evidence for two coeval magma suites from distinct sources: Journal of Petrology 46, 473–503.

Costa, F., Dohmen, R., & Chakraborty, S. (2008). Time scales of magmatic processes from modeling the zoning patterns of crystals. Reviews in Mineralogy and Geochemistry 69(1), 545-594.

Costa, F., Andreastuti, S., de Maisonneuve, C. B., & Pallister, J. S. (2013). Petrological insights into the storage conditions, and magmatic processes that yielded the centennial 2010 Merapi explosive eruption. Journal of Volcanology and Geothermal Research 261, 209-235.

Costa, F., Shea, T., & Ubide, T. (2020). Diffusion chronometry and the timescales of magmatic processes. Nature Reviews Earth & Environment, 1-14.

Davidson, J. P., Morgan, D. J., Charlier, B. L. A., Harlou, R. & Hora, J. M. (2007). Microsampling and isotopic analysis of igneous rocks: Implications for the study of magmatic systems. Annual Review of Earth and Planetary Sciences 35(1), 273-311.

Dick, H. J., & Bullen, T. (1984). Chromian spinel as a petrogenetic indicator in abyssal and alpine-type peridotites and spatially associated lavas. Contributions to Mineralogy and Petrology 86(1), 54-76.

Eggler, D. H. (1972). Water-saturated and undersaturated melting relations in a Paricutin andesite and an estimate of water content in the natural magma. Contributions to Mineralogy and Petrology 34(4), 261-271.

Erlund, E. J., Cashman, K. V., Wallace, P. J., Pioli, L., Rosi, M., Johnson, E., & Granados, H. D. (2010). Compositional evolution of magma from Parícutin Volcano, Mexico: The tephra record. Journal of Volcanology and Geothermal Research 197(1), 167-187.

Foshag, W. F., González-Reyna, J. (1956). Birth and development of Parícutin volcano, Mexico. U.S. Geological Survey Bulletin 965D, 355-485.

Fries Jr, C. (1953). Volumes and weights of pyroclastic material, lava, and water erupted by Paricutin volcano, Michoacan, Mexico. Eos, Transactions American Geophysical Union 34(4), 603-616.

Ginibre, C., Wörner, G. & Kronz, A. (2007). Crystal zoning as an archive for magma evolution. Elements 3(4), 261-266.

Girona, T., & Costa, F. (2013). DIPRA: A user-friendly program to model multi-element diffusion in olivine with applications to timescales of magmatic processes. Geochemistry, Geophysics, Geosystems 14(2), 422-431.

Gómez-Tuena, A., Orozco-Esquivel, M. T., & Ferrari, L. (2007). Igneous petrogenesis of the Trans-Mexican volcanic belt. Geological Society of America Special Papers 422, 129-181.

Gordeychik, B., Churikova, T., Kronz, A., Sundermeyer, C., Simakin, A., & Wörner, G. (2018). Growth of, and diffusion in, olivine in ultra-fast ascending basalt magmas from Shiveluch volcano. Scientific Reports, 8(1), 1-15.

Grove, T. L., Elkins-Tanton, L. T., Parman, S. W., Chatterjee, N., Müntener, O., & Gaetani, G. A. (2003). Fractional crystallization and mantle-melting controls on calc-alkaline differentiation trends. Contributions to Mineralogy and Petrology 145(5), 515-533.

Haase, K. M., & Renno, A. D. (2008). Variation of magma generation and mantle sources during continental rifting observed in Cenozoic lavas from the Eger Rift, Central Europe. Chemical Geology 257(3), 192-202.

Hasenaka, T., & Carmichael, I. S. (1985). The cinder cones of Michoacán—Guanajuato, central Mexico: Their age, volume and distribution, and magma discharge rate. Journal of Volcanology and Geothermal Research 25(1-2), 105-124.

Jankovics, M. É., Dobosi, G., Embey-Isztin, A., Kiss, B., Sági, T., Harangi, S. & Ntaflos, T. (2013). Origin and ascent history of unusually crystal-rich alkaline basaltic magmas from the western Pannonian Basin. Bulletin of Volcanology 75(9), 1-23.

Jankovics, M. É., Harangi, S., Németh, K., Kiss, B. & Ntaflos, T. (2015). A complex magmatic system beneath the Kissomlyó monogenetic volcano (western Pannonian Basin): evidence from mineral textures, zoning and chemistry. Journal of Volcanology and Geothermal Research 301, 38-55.

Jankovics, M. É., Sági, T., Astbury, R. L., Petrelli, M., Kiss, B., Ubide, T. & Harangi, S. (2019). Olivine major and trace element compositions coupled with spinel chemistry to unravel the magmatic systems feeding monogenetic basaltic volcanoes. Journal of Volcanology and Geothermal Research 369, 203-223.

Jerram, D. A. & Martin, V. M. (2008). Understanding crystal populations and their significance through the magma plumbing system. In: Annen, C., Zellmer, G. F. (eds) Dynamics of

crustal Magma Transfer, Storage and Differentiation. Geological Society of London Special Publication 304, 133-148.

Kahl, M., Chakraborty, S., Pompilio, M. & Costa, F. (2015). Constraints on the nature and evolution of the magma plumbing system of Mt. Etna Volcano (1991–2008) from a combined thermodynamic and kinetic modelling of the compositional record of minerals. Journal of Petrology 56, 2025–2068.

Kereszturi, G. & Németh, K. (2012). Monogenetic basaltic volcanoes: genetic classification, growth, geomorphology and degradation. In: Updates in volcanology-new advances in understanding volcanic systems. IntechOpen.

Larrea, P., França, Z., Lago, M., Widom, E., Galé, C., & Ubide, T. (2012). Magmatic processes and the role of antecrysts in the genesis of Corvo Island (Azores Archipelago, Portugal). Journal of Petrology 54(4), 769-793.

Larrea, P., Salinas, S., Widom, E., Siebe, C., & Abbitt, R. J. (2017). Compositional and volumetric development of a monogenetic lava flow field: The historical case of Paricutin (Michoacan, Mexico). Journal of Volcanology and Geothermal Research 348, 36-48.

Larrea, P., Widom, E., Siebe, C., Salinas, S., & Kuentz, D. (2019a). A re-interpretation of the petrogenesis of Paricutin volcano: Distinguishing crustal contamination from mantle heterogeneity. Chemical Geology 504, 66-82.

Larrea, P., Siebe, C., Juárez-Arriaga, E., Salinas, S., Ibarra, H., & Böhnel, H. (2019b). The ~AD 500–700 (Late Classic) El Astillero and El Pedregal volcanoes (Michoacán, Mexico): a new monogenetic cluster in the making? Bulletin of Volcanology 81(10), 59.

Le Bas, M. J., Le Maitre, R. W., Strckeisen, A., & Zanettin, B. (1986). A chemical classification of volcanic rocks based on the total alkali–silica diagram. Journal of Petrology 27, 745-750.

Luhr, J. F. (2001). Glass inclusions and melt volatile contents at Paricutin Volcano, Mexico. Contributions to Mineralogy and Petrology 142(3), 261-283.

Luhr, J. F., Simkin, T., 1993. Parícutin. In: The Volcano Born in a Mexican Cornfield. Geoscience Press, Phoenix, Arizona, (427 pp).

Maclennan, J. (2017). Bubble formation and decrepitation control the CO2 content of olivine-hosted melt inclusions. Geochemistry, Geophysics, Geosystems 18(2): 597-616.

Mahgoub, A. N., Böhnel, H., Siebe, C., Salinas, S., & Guilbaud, M-N. (2017). Paleomagnetically inferred ages of a cluster of Holocene monogenetic eruptions in the Tacámbaro-Puruarán area (Michoacán, México): implications for volcanic hazards. Journal of Volcanology and Geothermal Research 347, 360-370.

Mahgoub, A. N., Reyes-Guzmán, N., Böhnel, H., Siebe, C., Pereira, G., & Dorison, A. (2018). Paleomagnetic constraints on the ages of the Holocene Malpaís de Zacapu lava flow eruptions, Michoacán (Mexico): implications for archeology and volcanic hazards. The Holocene 28(2), 229-245.

McBirney, A. R., Taylor, H. P., & Armstrong, R. L. (1987). Paricutin re-examined: a classic example of crustal assimilation in calc-alkaline magma. Contributions to Mineralogy and Petrology 95(1), 4-20.

Moore, G., & Carmichael, I. S. E. (1998). The hydrous phase equilibria (to 3 kbar) of an andesite and basaltic andesite from western Mexico: constraints on water content and conditions of phenocryst growth. Contributions to Mineralogy and Petrology 130(3-4), 304-319.

McGee, L., Beier, C., Smith, I., & Turner, S. (2011). Dynamics of melting beneath a small-scale basaltic system: A U-Th-Ra study from Rangitoto volcano, Auckland volcanic field, New Zealand. Contributions to Mineralogy and Petrology 162, 547–563.

McGee, L. E., Millet, M. A., Smith, I. E. M., Németh, K. & Lindsay, J. M. (2012). The inception and progression of melting in a monogenetic eruption: Motukorea Volcano, the Auckland Volcanic Field, New Zealand. Lithos 155, 360–374.

Morgado, E., Morgan, D. J., Harvey, J., Parada, M. Á., Castruccio, A., Brahm, R., Harvey, J., Gutiérrez, F. & Hammond, S. J. (2019). Localised heating and intensive magmatic conditions prior to the 22–23 April 2015 Calbuco volcano eruption (Southern Chile). Bulletin of Volcanology 81(4), 24.

Ordóñez, E. (1947). El volcán Paricutín: México. Editorial Fantasía, México, 181 pp.

Pankhurst, M. J., Morgan, D. J., Thordarson, T., Loughlin, S. C. (2018). Magmatic crystal records in time, space, and process, causatively linked with volcanic unrest. Earth and Planetary Science Letters 493, 231-241.

Petry, C., Chakraborty, S., & Palme, H. (2004). Experimental determination of Ni diffusion coefficients in olivine and their dependence on temperature, composition, oxygen fugacity, and crystallographic orientation. Geochimica et Cosmochimica Acta, 68(20), 4179-4188.

Pioli, L., Erlund, E., Johnson, E., Cashman, K., Wallace, P., Rosi, M., & Granados, H. D. (2008). Explosive dynamics of violent Strombolian eruptions: the eruption of Parícutin Volcano 1943–1952 (Mexico). Earth and Planetary Science Letters 271(1-4), 359-368.

Putirka, K. D. (2008). Thermometers and barometers for volcanic systems. Reviews in mineralogy and geochemistry 69(1), 61-120.

Putirka, K., Johnson, M., Kinzler, R., Longhi, J., & Walker, D. (1996). Thermobarometry of mafic igneous rocks based on clinopyroxene-liquid equilibria, 0–30 kbar. Contributions to Mineralogy and Petrology 123(1), 92-108.

Re, G., Palin, J. M., White, J. D. L. & Parolari, M. (2017). Unravelling the magmatic system beneath a monogenetic volcanic complex (Jagged Rocks Complex, Hopi Buttes, AZ, USA). Contributions to Mineralogy and Petrology 172(11), 94.

Reid, M. R. (1979). Chemical Stratification of the Crust: Isotope, Trace Element, and Major Element Constraints from Crustally Contaminated Lavas and Lower Crustal Xenoliths. PhD Thesis. Massachusetts Institute of Technology (324 pp).

Reiners, P. W. (1998). Reactive melt transport in the mantle and geochemical signatures of mantle derived magmas. Journal of Petrology 39, 1039-1061.

Reubi, O. & Blundy, J. (2009). A dearth of intermediate melts at subduction zone volcanoes and the petrogenesis of arc andesites. Nature 461, 1269–1273.

Reyes-Guzmán, N., Siebe, C., Chevrel, M. O., Guilbaud, M. N., Salinas, S., & Layer, P. (2018). Geology and radiometric dating of Quaternary monogenetic volcanism in the western Zacapu lacustrine basin (Michoacán, México): implications for archeology and future hazard evaluations. Bulletin of Volcanology 80(2), 18.

Rowe, M. C., Peate, D. W., & Ukstins Peate, I. (2011). An investigation into the nature of the magmatic plumbing system at Paricutin Volcano, Mexico. Journal of Petrology 52(11), 2187-2220.

Scandone, R. (1979). Effusion rate and energy balance of Paricutin eruption (1943–1952), Michoacan, Mexico. Journal of Volcanology and Geothermal Research 6(1-2), 49-59.

Segerstrom, K. (1950). Erosion studies at Paricutin, state of Michoacan, Mexico. U.S. Geological Survey Bulletin 965-A, 164 pp.

Segerstrom, K., & Gutierrez, C. (1947). Activity of Parícutin volcano from May 4 to September 8, 1946. Eos, Transactions American Geophysical Union 28(4), 559-566.

Shane, P., Coote, A. (2018). Thermobarometry of Whangarei volcanic field lavas, New Zealand: Constraints on plumbing systems of small monogenetic basalt volcanoes. Journal of Volcanology and Geothermal Research 354, 130-139.

Shea, T., Lynn, K. J., & Garcia, M. O. (2015). Cracking the olivine zoning code: Distinguishing between crystal growth and diffusion. Geology 43(10), 935-938.

Smith, I. E. & Németh, K. (2017). Source to surface model of monogenetic volcanism: a critical review. In: Németh, K., Carrasco-Nuñez, G., Aranda-Gómez, J. J., Smith, I. E. M. (eds). Monogenetic Volcanism. Geological Society of London Special Publication 446, 1–28.

Smith, I. E. M., Blake, S., Wilson, C. J. N., & Houghton, B. F. (2008). Deep-seated fractionation during the rise of a small-volume basalt magma batch: Crater Hill, Auckland, New Zealand. Contributions to Mineralogy and Petrology 155(4), 511-527.

Sohn, Y. K., Cronin, S. J., Brenna, M., Smith, I. E. M., Németh, K., White, J. D. L., Murtagh, R.M., Jeon, Y.M., & Kwon, C. W. (2012). Ilchulbong tuff cone, Jeju Island, Korea, revisited: a compound monogenetic volcano involving multiple magma pulses, shifting vents, and discrete eruptive phases. Geological Society of America Bulletin 124(3-4), 259-274.

Streck, M. J. (2008). Mineral textures and zoning as evidence for open system processes. Reviews in Mineralogy and Geochemistry 69(1), 595-622.

Strong, M., & Wolff, J. (2003). Compositional variations within scoria cones. Geology 31(2), 143-146.

Sun, S. S., & McDonough, W. S. (1989). Chemical and isotopic systematics of oceanic basalts: implications for mantle composition and processes. Geological Society of London Special Publications 42(1), 313-345.

Toplis, M. J. (2005). The thermodynamics of iron and magnesium partitioning between olivine and liquid: criteria for assessing and predicting equilibrium in natural and experimental systems. Contributions to Mineralogy and Petrology 149, 22-39.

Ubide, T., Galé, C., Larrea, P., Arranz, E., & Lago, M. (2014). Antecrysts and their effect on rock compositions: the Cretaceous lamprophyre suite in the Catalonian Coastal Ranges (NE Spain). Lithos 206, 214-233.

Ubide, T. & Kamber, B. S. (2018). Volcanic crystals as time capsules of eruption history. Nature Communications 9(1), 326.

Van Otterloo, J., Raveggi, M., Cas, R. A. F., & Maas, R. (2014). Polymagmatic activity at the monogenetic Mt Gambier Volcanic Complex in the Newer Volcanics Province, SE Australia: new insights into the occurrence of intraplate volcanic activity in Australia. Journal of Petrology 55(7), 1317-1351.

Venugopal, S., Schiavi, F., Moune, S., Bolfan-Casanova, N., Druitt, T., & Williams-Jones, G. (2020). Melt inclusion vapour bubbles: the hidden reservoir for major and volatile elements. Scientific Reports, 10(1), 1-14.

Whitney, D. L., & Evans, B. W. (2010). Abbreviations for names of rock-forming minerals. American mineralogist, 95(1), 185-187.

Wilcox, R. E. (1954). Petrology of Parícutin Volcano Mexico. U.S. Geological Survey Bulletin 965C, 281–353.

Wilcox, R. E., & Gutiérrez, C. (1948). Activity of Parícutin volcano from April 1 to July 31, 1948. Eos, Transactions American Geophysical Union 29(6), 877-881.

Yokoyama, I., & De la Cruz-Reyna, S. (1990). Precursory earthquakes of the 1943 eruption of Paricutin volcano, Michoacan, Mexico. Journal of Volcanology and Geothermal Research 44(3-4), 265-281.

Zellmer, G. F., Sakamoto, N., Matsuda, N., Iizuka, Y., Moebis, A., & Yurimoto, H. (2016). On progress and rate of the peritectic reaction Fo+ SiO_2→ En in natural andesitic arc magmas. Geochimica et Cosmochimica Acta 185, 383-393.

FIGURE CAPTIONS

Fig. 1. (a) Geotectonic map of Mexico with the location of the Trans-Mexican Volcanic Belt (TMVB; reddish polygon). The Michoacán-Guanajuato Volcanic Field (MGVF; Hasenaka and Carmichael, 1985) is within black quadrangle, and the location of Paricutin (P) is denoted by a red pentagon. Major fracture zones are indicated by black lines and include: TFZ= Tamayo Fracture Zone, RFZ= Rivera Fracture Zone, OFZ= Orozco fracture Zone, and the MAT= Middle America Trench. (b) Geological map of Paricutin volcano (created using ArcGIS® software) with the 23 eruptive phases modified after Larrea et al. (2017) and Luhr & Simkin (1993) spanning the 9 years of eruption, including the lava (circle) and tephra (square) samples studied by Larrea et al. (2019a) and those labeled are the ones studied here. The same colors and symbols are used in the following figures. See web version for colors.

Fig. 2. (a) Total alkalis vs. SiO_2 (TAS) diagram (after Le Bas et al., 1986), (b) Mg# [Mg#= 100xMg/(Mg+Fe^T) where Fe^T includes total iron as Fe^{2+}] vs. eruption timeline, and (c-d) selected whole rock major element vs. SiO_2 (wt %) for Paricutin tephra (T, square) and lava flows (L, circle) throughout the eruption (Larrea et al., 2019a). Note that samples analyzed for mineral chemistry in this study are labelled in b-d) by tephra or lava flow number (eruptive phase). Tephra and lava samples analyzed by Cebriá et al. (2011), Erlund et al. (2010), McBirney et al. (1987), Luhr (2001), Reid (1979), Rowe et al. (2011), and Wilcox (1954) are included as black symbols. Legend as in Fig. 1; See web version for colors.

Fig. 3. Optical microscope images of Paricutin samples in cross- (upper left) and plain-polarized (lower right) transmitted light: (a) tephra T1, (b) tephra T3, (c) lava L3, (d) lava L14, (e) lava L20, and (f) lava L22. Note that the macrocryst assemblage changes with time and melt whole

rock composition (see details in the text); the groundmass is composed of feldspar, olivine (Ol), orthopyroxene (Opx), clinopyroxene, (Ti-) magnetite microcrysts, and minor glass. Mineral abbreviations according to Whitney & Evans (2010). See web version for colors.

Fig. 4. Back-scattered electron (BSE) microscope images of representative mineral textures in the early tephra T1-T2 vs. tephra T3-T4 and lava samples. BSE images of (a-d) olivine, (e, g-h) orthopyroxene (Opx), (f) clinopyroxene (Cpx), (i, k) feldspar (Fsp), and (j, l) Cr-spinel (Cr-Sp) crystals included in olivine macrocrysts. Insets in (c), (d), and (j) are detailed BSE images of orthopyroxene outer rim and symplectitic outer rims around olivine, and zoned Cr-spinel, respectively. Also note magnetite microcrysts within the groundmass in (a-l). See X-Ray compositional maps and BSE images of (b), (e) and (j) in Albert et al. (2020). Mineral abbreviations according to Whitney & Evans (2010).

Fig. 5. Variation in mineral compositions with time for the analyzed crystals in Paricutin tephra and lavas: (a) olivine (Ol) - Fo# [Fo#= 100xMg/(Mg+Fe^{2+}) atomic ratio], (b) orthopyroxene (Opx) - Mg# [Mg#= 100xMg/(Mg+Fe^{2+}) atomic ratio], (c) clinopyroxene (Cpx) - Mg#[Mg#= 100xMg/(Mg+Fe^{2+}+Fe^{3+}) atomic ratio], (d) feldspar (Fsp) – An [An= 100xCa/(Ca+Na+K) atomic ratio], and (e) spinel (Sp) – Mg# [Mg#= Mg/(Mg+Fe^{2+}) atomic ratio]. The diagram includes core-to-rim traverses in olivine, orthopyroxene, and feldspar macrocrysts, and individual spot analyses in microcrysts and some macrocrysts. Crystals are classified as tephra macrocrysts (squares), tephra microcrysts (crosses), lava macrocrysts (circles), and lava microcrysts (diagonal crosses). Mineral abbreviations according to Whitney & Evans (2010). See web version for colors.

Fig. 6. (a) Olivine - Fo#, (b) clinopyroxene – Mg#, and (c) orthopyroxene – Mg# (calculated as in Fig. 5) vs. Mg# in whole rock. The diagram includes core-to-rim traverses in olivine, clinopyroxene, and orthopyroxene, and individual spot analyses in microcrysts and some macrocrysts. Curves represent the range of equilibrium compositions between mineral and melt

using an Fe-Mg distribution coefficient of 0.34 ± 0.02 for olivine (Erlund et al., 2010), 0.28 ± 0.08 for clinopyroxene, and 0.29 ± 0.06 for orthopyroxene according to Putirka (2008). For (a) and (c) the whole rock Mg# was calculated as $Mg/(Mg+Fe^{2+})$, where the Fe^{2+}/Fe^{3+} ratio was calculated at QFM+1, whereas for (c) whole rock Mg#= $100xMg/(Mg+Fe^{T})$ where Fe^{T} includes total iron as Fe^{2+}. Insets show the core-to-rim chemical variation of selected tephra and lava crystals with highlighted equilibrium range (pink polygon). Blue arrows in (a) indicate chemical variation in normally zoned crystals from core to rim. See web version for colors. (d) Mg# [$Mg/(Mg+Fe^{2+})$ atomic ratio] vs. Cr# [Cr/(Cr+Al) atomic ratio] compositional variations of Cr-spinel and (Ti-) magnetite from Paricutin tephra and lava. Dashed lines in (d) denote the composition of olivine in equilibrium with Cr-spinel at a nominal temperature of 1,200 ºC (Dick & Bullen, 1984). The color-coding of the symbols refers to the eruptive phase.

Fig. 7. Thermobarometry estimates, including kernel density estimation, from orthopyroxene macrocrysts-whole rock melt equilibria. Orthopyroxene pressures were obtained with the Eq. 29a barometer, and temperatures were calculated with the Eq. 28a thermometer of Putirka et al. (2008). Note that for all calculations 3 wt % H_2O were assumed. See web version for colors.

Fig. 8. (a) Compositional profiles from core to rim and diffusion models for two representative olivine crystals from L3 and L23. Black and white diamonds are Fo# and NiO (wt %) concentrations, respectively. Green lines are the initial profile shapes and boundaries. Red lines are the best-fit diffusion models computed using DIPRA (Girona & Costa, 2013). (b) Summary of calculated times in days obtained by modelling the chemical diffusion of Fe–Mg and Ni in olivine crystals from L3, L7, L20, and L23. Errors shown are reported in Table 1. See web version for colors.

Fig. 9. Correlation between the eruption dates for L3, L7, L20, and L23 and the calculated timescales for the olivine crystals contained in each lava (diamonds are Fo# and Ni timescales

with error bars as in Fig. 8). Note that olivine timescales are in accordance with the arrival of a new batch of magma before the eruption of each lava flow.

Fig. 10. Schematic representation of the Paricutin plumbing system showing the main characteristics of the volcanic products erupted during a) the "system opening" stage, and b) the "steady-state" stage. Green crystals represent olivine, while black and white are feldspar.

TABLES

Table 1. Timescales (in days) calculated by modeling the chemical diffusion of Fe–Mg and Ni in olivine crystals (see modeling parameters in Table VI of the Electronic Appendix 1). Plateau 1 and 2 are the two compositional plateaus used as boundary conditions, and Δ(−) and Δ(+) are the errors on the total time calculated by DIPRA (Girona & Costa, 2013) after the anisotropy correction.

ELECTRONIC APPENDIX 1 - TABLES

Electronic supplements for this paper are available at Journal of Petrology online.

Table I. Chemical composition of olivine crystals (macrocrysts and microcrysts) in tephra and lavas analyzed by electron probe micro-analysis (EPMA).

Table II. Chemical composition of orthopyroxene crystals (macrocrysts and microcrysts) in tephra and lavas analyzed by electron probe micro-analysis (EPMA).

Table III. Chemical composition of clinopyroxene crystals (macrocrysts and microcrysts) in tephra and lavas analyzed by electron probe micro-analysis (EPMA).

Table IV. Chemical composition of feldspar crystals (macrocrysts and microcrysts) in tephra and lavas analyzed by electron probe micro-analysis (EPMA).

Table V. Chemical composition of spinel crystals (microcrysts) in tephra and lavas analyzed by electron probe micro-analysis (EPMA).

Table VI. Initial and boundary conditions, and uncertainty of diffusion times that account for analytical, temperature, and oxygen fugacity uncertainties as calculated by DIPRA (Girona & Costa, 2013) after the anisotropy correction.

ELECTRONIC APPENDIX 2 – MINERAL CHEMISTRY: TEXT AND FIGURES

ELECTRONIC APPENDIX 3 – OLIVINE MAXIMUM TIMESCALE MODELLING: TEXT AND FIGURES

Table 1. Maximum timescales (in days) calculated by modeling the chemical diffusion of Fe–Mg and Ni in olivine crystals. Plateau 1 and rim are the two boundary conditions, and Δ(−) and Δ(+) are the errors on the total time calculated by DIPRA (Girona & Costa, 2013) after the anisotropy correction. *Note olivine PAR-1215-1 from L3 as one of the few crystals with a more complex zoning with two plateaus (see details in Electronic Appendix 3).

Lava Sample	Olivine	Element	Time (days)	Plateau 1	Rim	Δ (-)	Δ(+)	Discrepancy (%)
PAR-1215 L3*	1215-1	Fo	141.9	82.7	76.2	37.76	51.69	1
	1215-1	Ni	97.31	0.41	0.23	51.81	57.35	7
	1215-1	Fo	146.2	82.3	76.2	40.93	51.2	2
	1215-2	Fo	171.2	82.2	77.3	39.52	52.48	3
	1215-2	Ni	62.62	0.35	0.26	40.71	64.15	<1
	1215-3	Fo	451.4	81.34	77.4	165.7	167.8	6
	1215-3	Ni	149.8	0.30	0.24	122.5	63.3	6
	1215-10	Fo	222.8	82.5	76.9	80.54	104.3	<1
	1215-10	Ni	74.25	0.35	0.23	42.6	59.25	2
PAR-1216 L7	1216-1	Fo	84.95	83.8	74.6	25.77	30.27	3
	1216-1	Ni	254.3	0.42	0.19	90.27	145.9	21
	1216-2	Fo	37.96	82.3	76.5	12.84	20.33	<1
PAR-1524 L20	1524-1	Fo	31.86	78.5	73.5	10.95	16.67	8
	1524-2	Fo	173	78.4	75.9	99.11	93.02	<1
	1524-6	Fo	105	78.6	76.6	76.42	68.88	4
	1524-6	Ni	18.23	0.27	0.25	22.98	127.3	4
PAR-1520 L23	1520-5b	Fo	49.86	79.8	72.4	13.49	19.11	11
	1520-7	Fo	288.2	79.3	72.3	99.51	114.6	<1
	1520-7	Ni	221.9	0.30	0.25	252.7	206.5	<1
	1520-10	Fo	12.13	79.7	77.6	8.536	8.119	<1
	1520-12	Fo	26.6	79.7	71.0	7.623	9.179	7
	1520-12	Ni	10.38	0.31	0.25	13.09	35.08	<1

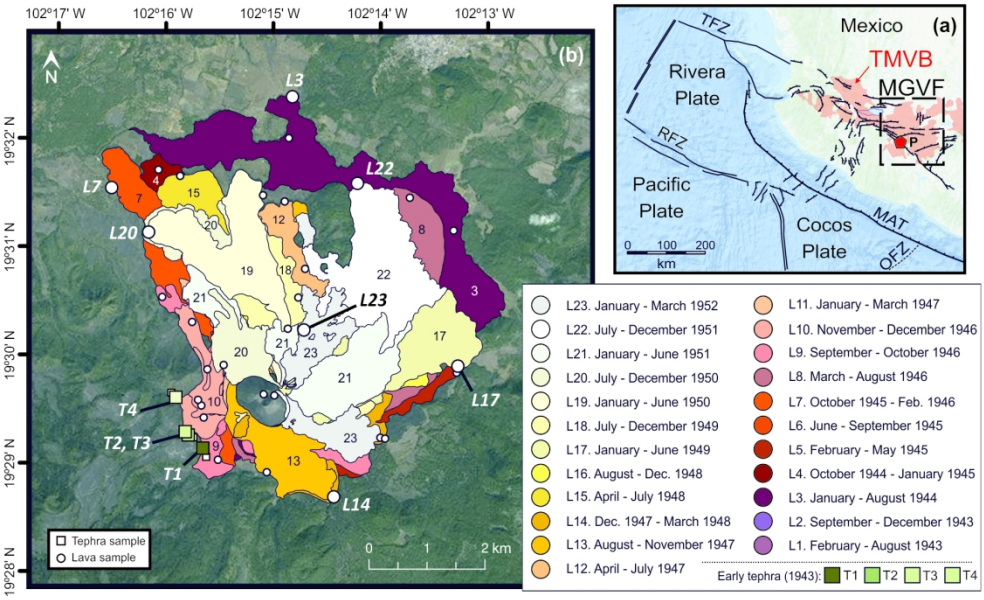

Fig. 1. (a) Geotectonic map of Mexico with the location of the Trans-Mexican Volcanic Belt (TMVB; reddish polygon). The Michoacán-Guanajuato Volcanic Field (MGVF; Hasenaka and Carmichael, 1985) is within black quadrangle, and the location of Paricutin (P) is denoted by a red pentagon. Major fracture zones are indicated by black lines and include: TFZ= Tamayo Fracture Zone, RFZ= Rivera Fracture Zone, OFZ= Orozco fracture Zone, and the MAT= Middle America Trench. (b) Geological map of Paricutin volcano (created using ArcGIS® software) with the 23 eruptive phases modified after Larrea et al. (2017) and Luhr & Simkin (1993) spanning the 9 years of eruption, including the lava (circle) and tephra (square) samples studied by Larrea et al. (2019a) and those labeled are the ones studied here. The same colors and symbols are used in the following figures.

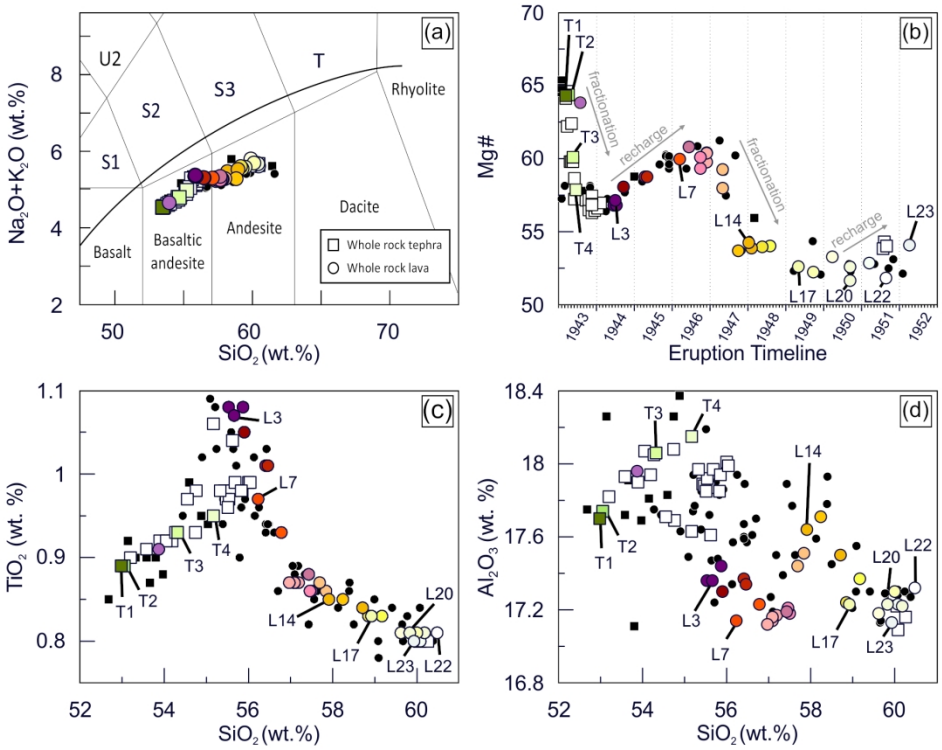

Fig. 2. (a) Total alkalis vs. SiO2 (TAS) diagram (after Le Bas et al., 1986), (b) Mg# [Mg#= 100xMg/(Mg+FeT) where FeT includes total iron as Fe2+] vs. eruption timeline, and (c-d) selected whole rock major element vs. SiO2 (wt %) for Paricutin tephra (T, square) and lava flows (L, circle) throughout the eruption (Larrea et al., 2019a). Note that samples analyzed for mineral chemistry in this study are labelled in b-d) by tephra or lava flow number (eruptive phase). Tephra and lava samples analyzed by Cebriá et al. (2011), Erlund et al. (2010), McBirney et al. (1987), Luhr (2001), Reid (1979), Rowe et al. (2011), and Wilcox (1954) are included as black symbols. Legend as in Fig. 1.

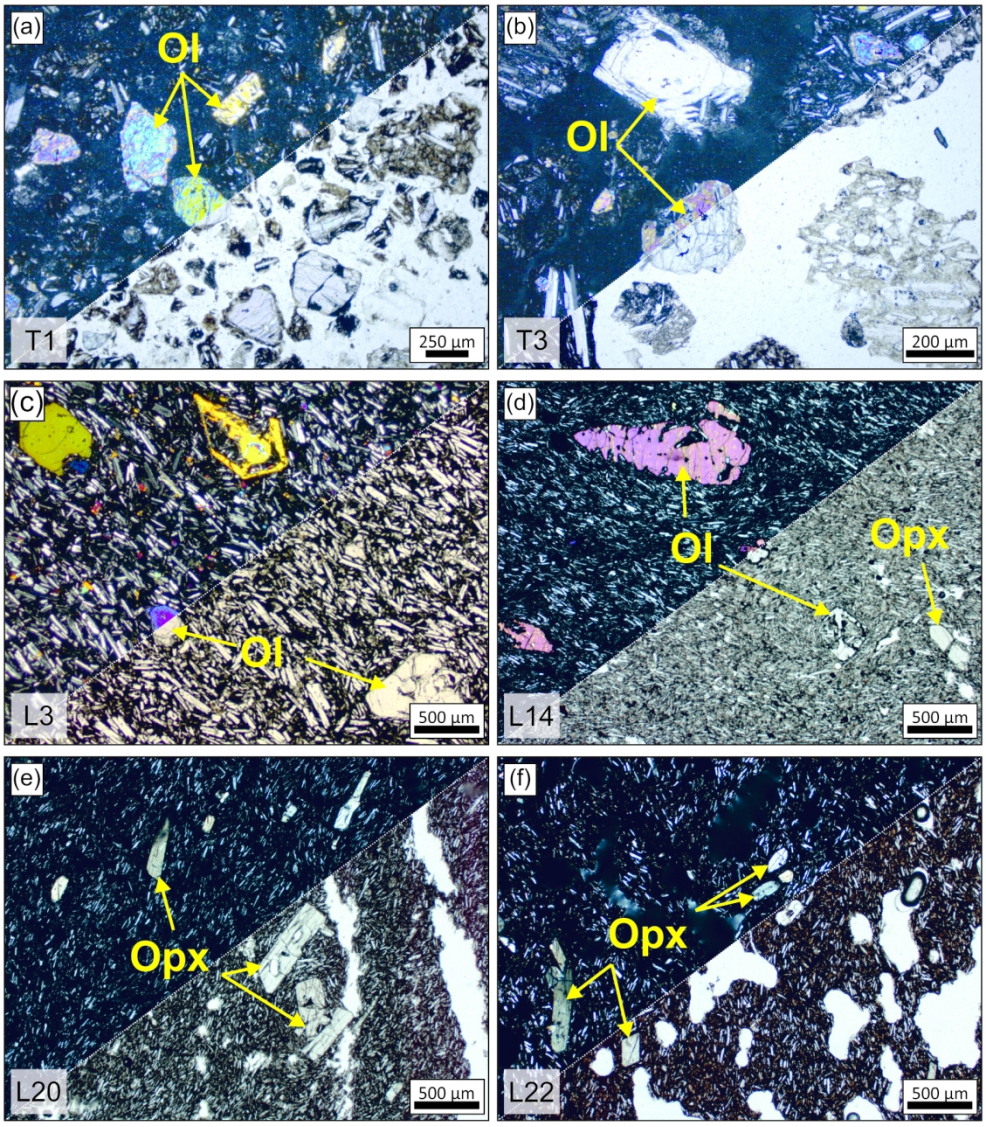

Fig. 3. Optical microscope images of Paricutin samples in cross- (upper left) and plain-polarized (lower right) transmitted light: (a) tephra T1, (b) tephra T3, (c) lava L3, (d) lava L14, (e) lava L20, and (f) lava L22. Note that the macrocryst assemblage changes with time and melt whole rock composition (see details in the text); the groundmass is composed of feldspar, olivine (Ol), orthopyroxene (Opx), clinopyroxene, (Ti-) magnetite microcrysts, and minor glass. Mineral abbreviations according to Whitney & Evans (2010).

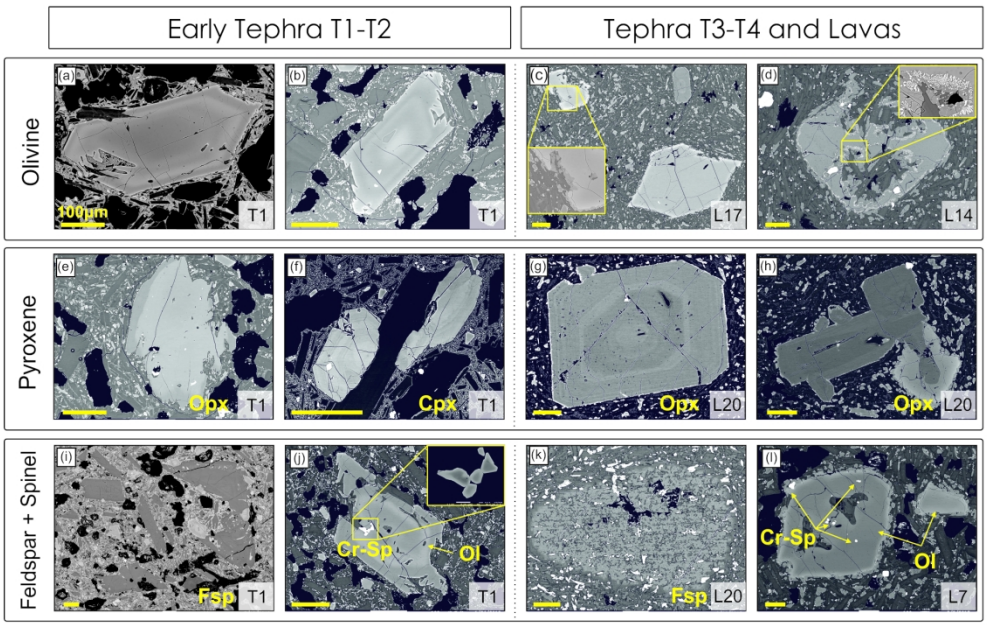

Fig. 4. Back-scattered electron (BSE) microscope images of representative mineral textures in the early tephra T1-T2 vs. tephra T3-T4 and lava samples. BSE images of (a-d) olivine, (e, g-h) orthopyroxene (Opx), (f) clinopyroxene (Cpx), (i, k) feldspar (Fsp), and (j, l) Cr-spinel (Cr-Sp) crystals included in olivine macrocrysts. Insets in (c), (d), and (j) are detailed BSE images of orthopyroxene outer rim and symplectitic outer rims around olivine, and zoned Cr-spinel, respectively. Also note magnetite microcrysts within the groundmass in (a-l). See X-Ray compositional maps and BSE images of (b), (e) and (j) in Albert et al. (2020). Mineral abbreviations according to Whitney & Evans (2010).

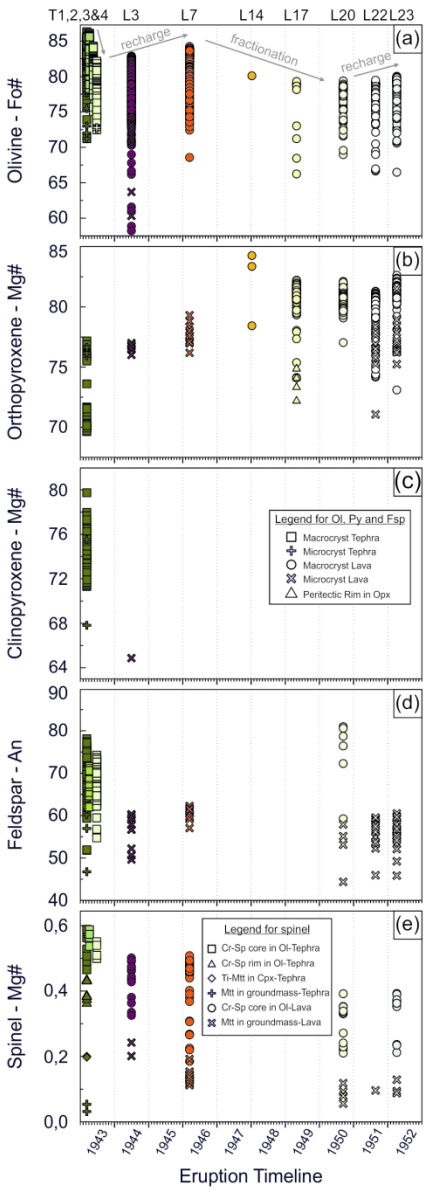

Fig. 5. Variation in mineral compositions with time for the analyzed crystals in Paricutin tephra and lavas: (a) olivine (Ol) - Fo# [Fo#= 100xMg/(Mg+Fe2+) atomic ratio], (b) orthopyroxene (Opx) - Mg# [Mg#= 100xMg/(Mg+Fe2+) atomic ratio], (c) clinopyroxene (Cpx) - Mg#[Mg#= 100xMg/(Mg+Fe2++Fe3+) atomic ratio], (d) feldspar (Fsp) – An [An= 100xCa/(Ca+Na+K) atomic ratio], and (e) spinel (Sp) – Mg# [Mg#= Mg/(Mg+Fe2+) atomic ratio]. The diagram includes core-to-rim traverses in olivine, orthopyroxene, and feldspar macrocrysts, and individual spot analyses in microcrysts and some macrocrysts. Crystals are classified as tephra macrocrysts (squares), tephra microcrysts (crosses), lava macrocrysts (circles), and lava microcrysts (diagonal crosses). Mineral abbreviations according to Whitney & Evans (2010).

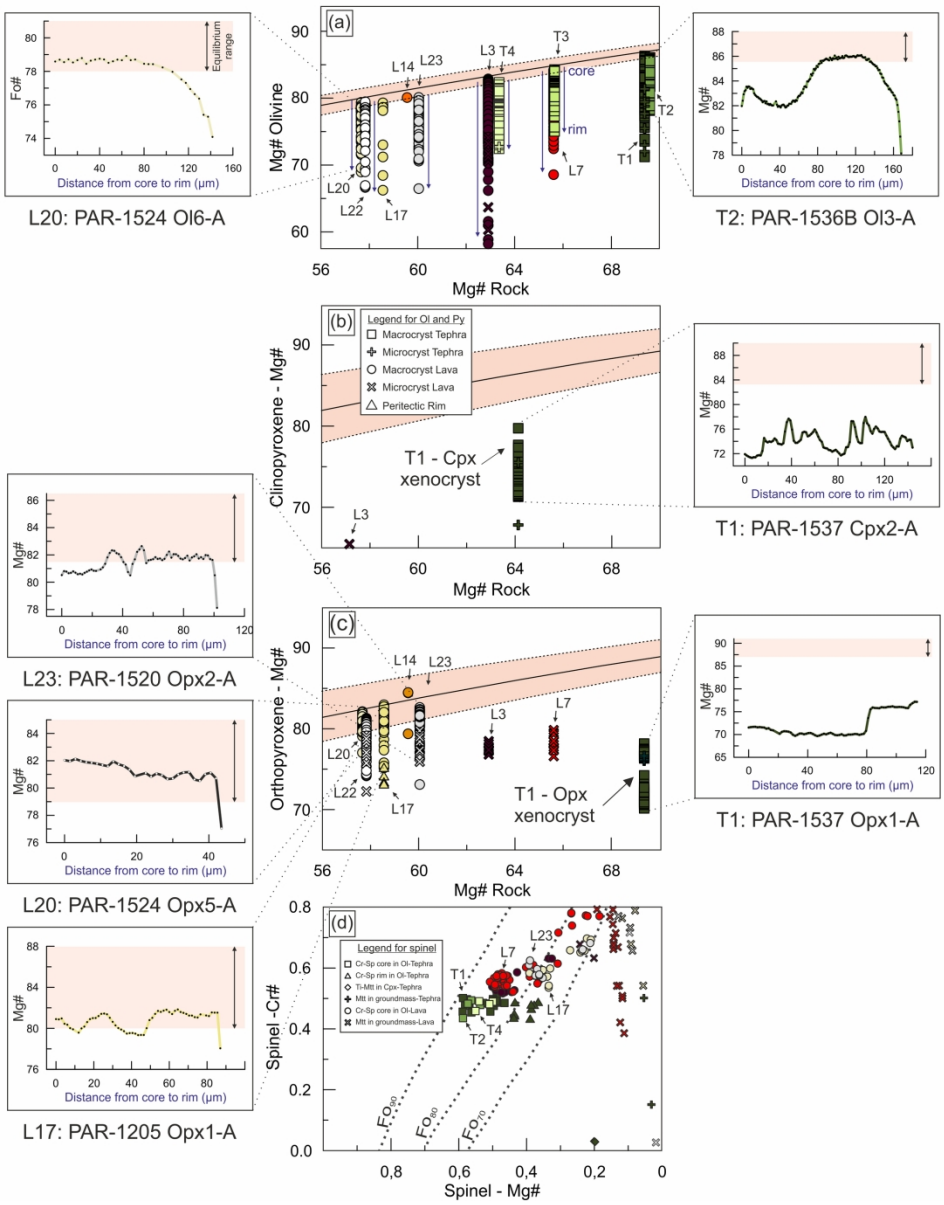

Fig. 6. (a) Olivine - Fo#, (b) clinopyroxene – Mg#, and (c) orthopyroxene – Mg# (calculated as in Fig. 5) vs. Mg# in whole rock. The diagram includes core-to-rim traverses in olivine, clinopyroxene, and orthopyroxene, and individual spot analyses in microcrysts and some macrocrysts. Curves represent the range of equilibrium compositions between mineral and melt using an Fe-Mg distribution coefficient of 0.34 ± 0.02 for olivine (Erlund et al., 2010), 0.28 ± 0.08 for clinopyroxene, and 0.29 ± 0.06 for orthopyroxene according to Putirka (2008). For (a) and (c) the whole rock Mg# was calculated as Mg/(Mg+Fe2+), where the Fe2+/Fe3+ ratio was calculated at QFM+1, whereas for (c) whole rock Mg#= 100xMg/(Mg+FeT) where FeT includes total iron as Fe2+. Insets show the core-to-rim chemical variation of selected tephra and lava crystals with highlighted equilibrium range (pink polygon). Blue arrows in (a) indicate chemical variation in normally zoned crystals from core to rim. See web version for colors. (d) Mg# [Mg/(Mg+Fe2+) atomic ratio] vs. Cr# [Cr/(Cr+Al) atomic ratio] compositional variations of Cr-spinel and (Ti-) magnetite from Paricutin tephra and lava. Dashed lines in (d) denote the composition of olivine in equilibrium with Cr-spinel at a nominal temperature of 1,200 ºC (Dick & Bullen, 1984). The color-coding of the symbols refers to the eruptive phase.

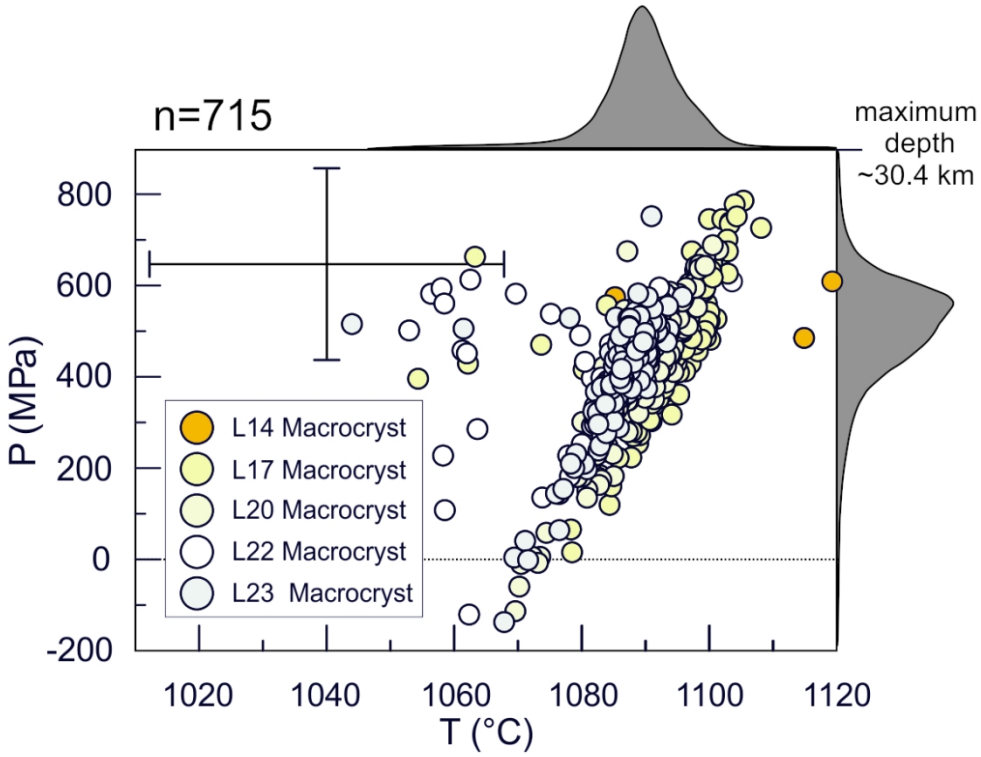

Fig. 7. Thermobarometry estimates, including kernel density estimation, from orthopyroxene macrocrysts-whole rock melt equilibria. Orthopyroxene pressures were obtained with the Eq. 29a barometer, and temperatures were calculated with the Eq. 28a thermometer of Putirka et al. (2008). Note that for all calculations 3 wt % H2O were assumed.

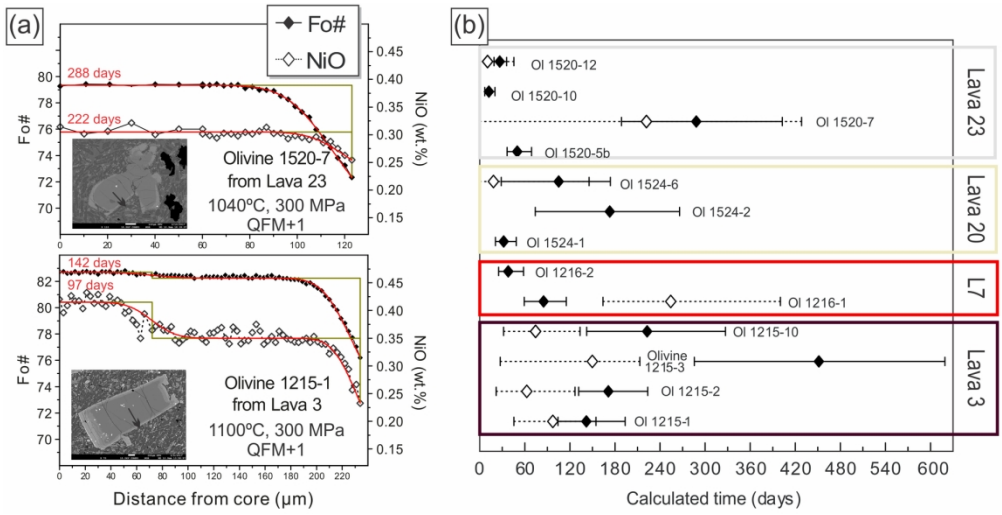

Fig. 8. (a) Compositional profiles from core to rim and diffusion models for two representative olivine crystals from L3 and L23. Black and white diamonds are Fo# and NiO (wt %) concentrations, respectively. Green lines are the initial profile shapes and boundaries. Red lines are the best-fit diffusion models computed using DIPRA (Girona & Costa, 2013). (b) Summary of calculated times in days obtained by modelling the chemical diffusion of Fe–Mg and Ni in olivine crystals from L3, L7, L20, and L23. Errors shown are reported in Table 1.

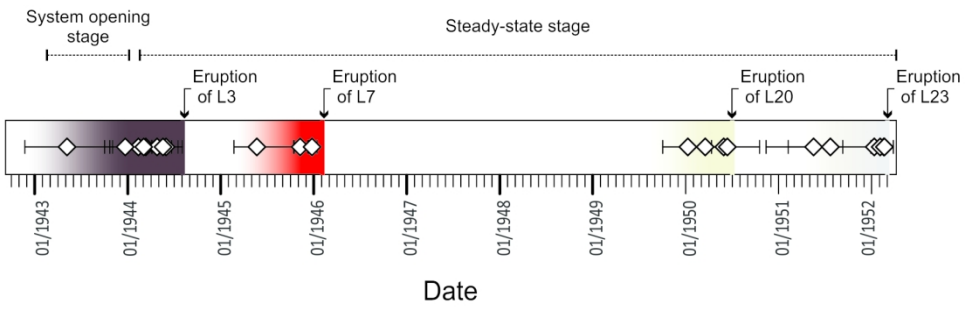

Fig. 9. Correlation between the eruption dates for L3, L7, L20, and L23 and the calculated timescales for the olivine crystals contained in each lava (diamonds are Fo# and Ni timescales with error bars as in Fig. 8). Note that olivine timescales are in accordance with the arrival of a new batch of magma before the eruption of each lava flow.

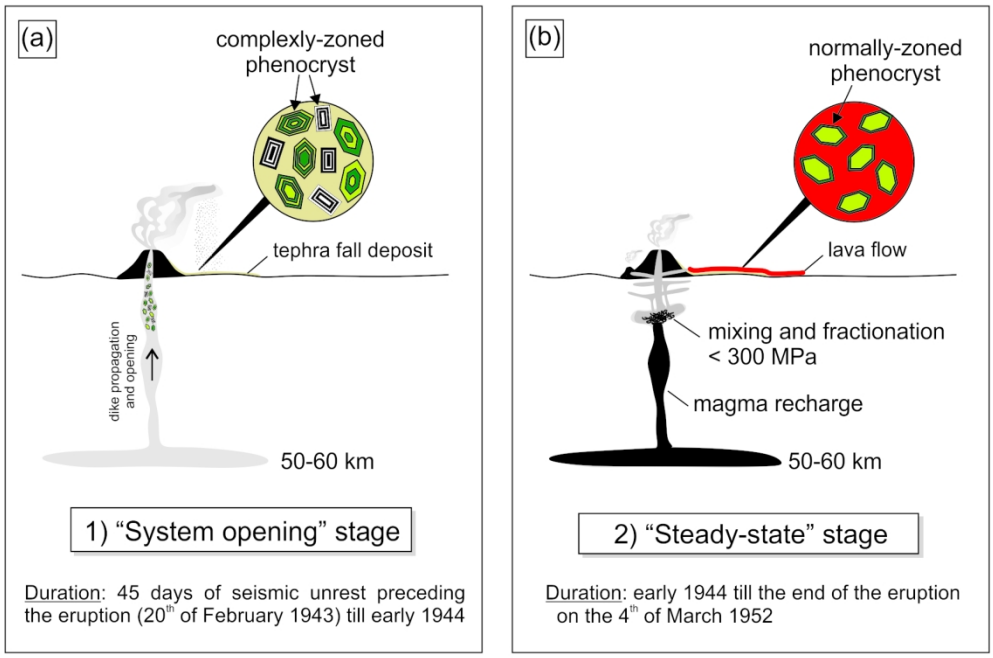

Fig. 10. Schematic representation of the Paricutin plumbing system, showing the main characteristics of the volcanic products erupted during a) the “system opening” stage, and b) the “steady-state” stage. Green crystals represent olivine, while black and white are feldspar.